I&EC research
Industrial & Engineering Chemistry Research

pubs.acs.org/IECR

Article

Kinetics, Model Discrimination, and Parameters Estimation of CO_2 Methanation on Highly Active Ni/CeO_2 Catalyst

Jon A. Onrubia-Calvo, Adrián Quindimil, Arantxa Davó-Quiñonero, Alejandro Bermejo-López, Esther Bailón-García, Beñat Pereda-Ayo, Dolores Lozano-Castelló, José A. González-Marcos, Agustín Bueno-López, and Juan R. González-Velasco*

Cite This: *Ind. Eng. Chem. Res.* 2022, 61, 10419−10435

Read Online

ACCESS | Metrics & More | Article Recommendations | Supporting Information

ABSTRACT: The reaction kinetics of CO_2 methanation over a highly active 8.5% Ni/CeO_2 catalyst was determined in a fixed-bed reactor, in the absence of heat- and mass-transfer limitations. Once the catalyst activity was stabilized, more than 120 kinetic experiments (with varying values of reaction temperature, total pressure, space velocity (GHSV), and partial pressure of products and reactants) were performed. From initial reaction rates, an apparent activation energy of 103.9 kJ mol^{-1} was determined, as well as the effect of reactants (positive) and water partial pressures (negative) on CO_2 methanation rate. Three mechanistic models reported in the literature, in which CO_2 is adsorbed dissociatively (carbon and formyl routes) or directly (formate route), were explored for modeling the entire reaction kinetics. For that, the corresponding rate equations were developed through the Langmuir−Hinshelwood−Hougen−Watson (LHHW) approach. In agreement with DRIFTS experiments, formate route, in which the hydrogenation of bicarbonate to formate is considered to be the rate-determining step, reflects the kinetic data accurately, operating from differential conversion to thermodynamic equilibrium. In fact, this mechanism results in a mean deviation (D) of 10.38%. Based on previous own mechanistic studies, the participation of two different active sites has been also considered. Formate route on two active sites maintains a high fitting quality of experimental data, providing kinetics parameters with a higher physical significance. Thus, the LHHW mechanism, in which Ni^0 sites as well as oxygen vacant near to Ni-CeO_2 interface participate in CO_2 methanation, is able to predict the kinetics of Ni/CeO_2 catalyst accurately for a wide range of operational conditions.

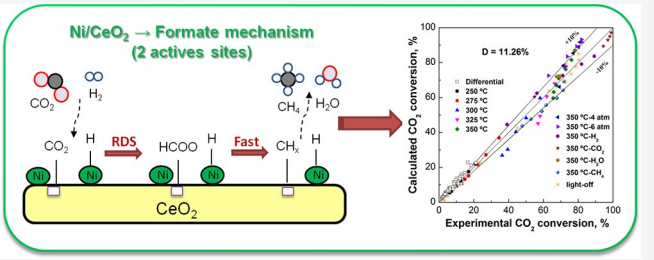

1. INTRODUCTION

The steep rise in the energy consumption derived from the accelerated population increase has led to an extensive exploitation of fossil fuels. The consumption of this energy source releases tons of CO_2 emissions, which is one of the major components of greenhouse gases (GHG) emitted into the Earth's atmosphere, causing global warming and climate change.[1,2] Considering the negative impact of CO_2 emission on global climate change, leading CO_2-emitting countries have pledged to cut CO_2 emissions significantly in the near future to limit the temperature increase to 1.5 °C above preindustrial levels. In this context, the transition to renewable energies will be a key factor.[3] However, their intermittence, in contrast to conventional power plants, as well as its preferred generation in remote areas, leading to a storage necessity, emerge as two critical challenges.

Power-to-gas (PtG) technology is a practical and convenient alternative to leverage excess of electricity by conversion into the so-called chemical energy carriers, such as H_2 or CH_4. The latter, also known as power-to-methane (PtM) technology, is based on the capture and utilization of CO_2 (CCU) as a raw material, for the production of CH_4 with the renewable H_2 produced by H_2O electrolysis, using the excess of electricaity produced by renewable energies. Thus, the PtM alternative contributes to mitigate CO_2 emissions and allows storaging the excess of the electrical energy as grid-compatible renewable natural gas.[4]

The heart of the PtM concept is the CO_2 methanation via the Sabatier reaction (eq 1):[5]

$$CO_2 + 4H_2 \leftrightarrows CH_4 + 2H_2O \qquad \Delta H_{298K} = -165\ \text{kJ mol}^{-1} \tag{1}$$

CO_2 methanation is a very exothermic reaction with volume contraction; thus, it is thermodynamically favored at low temperatures and high pressures.[6] However, the CO_2 methanation reaction presents a strong kinetic barrier, because

Special Issue: Engineered Methodologies for CO2 Utilization

Received: January 13, 2022
Revised: April 20, 2022
Accepted: April 30, 2022
Published: May 20, 2022

Table 1. Overview of Kinetics Models Presented in the Literature

catalyst (Ni wt %)	T (°C)	P (bar)	rate equation	ref
Ni/CeO_2 nanorods and nanocubes (5.0)	210−240	1	$r_{CH_4} = \frac{k_4 K_{H_2}^{0.5} K_{OH} K_{CO_2} p_{H_2}^{0.5} p_{CO_2}}{\left(1 + \frac{k K_{H_2}^{0.5} K_{OH} K_{CO_2}}{k_6} p_{H_2}^{-0.5} p_{CO_2}^{2}\right)^2}$	8
Ni/CeO_2 modified with C_3N_4 (6.0)	210−240	1	$r_{CH_4} = \frac{k K_{H_2}^{0.5} K_{OH} K_{CO_2} p_{CO_2} p_{H_2}^{0.5}}{\left(1 + K_{H_2}^{0.5} K_{OH} p_{H_2}^{0.5} + K_{CO_2} p_{CO_2}\right)^2 \left\{[O^*](1 + K_{CO_2} p_{CO_2} + K_{H_2}^{0.5} K_{OH} p_{H_2}^{0.5})\right\}^2}$	41
Ni/SiO_2 (58)	275−320	17	$r_{CH_4} = k p_{CO_2}^{0.66} p_{H_2}^{0.21}$	34
Ni/SiO_2 (60)	280−400	30	$r_{CH_4} = \frac{k p_{CO_2} p_{H_2}^{4}}{\left(1 + K_{H_2} p_{H_2} + K_{CO_2} p_{CO_2}\right)^5}$	37
Ni/SiO_2 (3)	227−327	0.16	$r_{CH_4} = \frac{k p_{CO_2}^{0.5} p_{H_2}^{0.5}}{\left[1 + K_1 p_{CO_2}^{0.5} p_{H_2}^{0.5} + K_2\left(\frac{p_{CO_2}^{0.5}}{p_{H_2}^{0.5}}\right) + K_3 p_{CO}\right]^2}$	38
$NiAl(O)_x$(0.37−5.5 Ni/Al molar ratios)	180−340	1−15	$r = \frac{k p_{H_2}^{0.5} p_{CO_2}^{0.5}\left(1 - \frac{p_{CH_4} p_{H_2O}^{2}}{p_{CO_2} p_{H_2}^{4} K_{eq}}\right)}{\left[1 + K_{H_2} p_{H_2}^{0.5} + K_{OH}\left(\frac{p_{H_2O}}{p_{H_2}^{0.5}}\right) + K_{mix} p_{CO_2}^{0.5}\right]^2}$	45
Ni/Al hydrotalcite (75)	270−390	1	$r = \frac{k p_{H_2}^{0.5} p_{CO_2}^{0.5}\left(1 - \frac{p_{CH_4} p_{H_2O}^{2}}{p_{CO_2} p_{H_2}^{4} K_{eq}}\right)}{\left[1 + \sqrt{K_{H_2} p_{H_2}} + K_{OH}\left(\frac{p_{H_2O}}{p_{H_2}^{0.5}}\right) + K_{mix} p_{CO_2}^{0.5}\right]^2}$	48
Ni/Al_2O_3 (14−17)	350−450	1	$r_{CH_4} = \frac{k K_{H_2O} K_{CO_2} p_{CO_2}\left(1 - \frac{p_{CH_4} p_{H_2O}^{2}}{p_{H_2}^{4} p_{CO_2} K_{eq}}\right)}{(1 + K_{CO_2} p_{CO_2} + K_{H_2} p_{H_2} + K_{H_2O} p_{H_2O} + K_{CO} p_{CO})^2}$	49
Ni/Al_2O_3 (28)	200−230	1	$r_{CH_4} = \frac{k p_{CO_2}}{1 + A_{CO_2} p_{CO_2}}$	50
Ni/Al_2O_3 (30)	320−420	1.2−7.3	$r_{CH_4} = \frac{k_1 K_{HCOO} P_{CO_2} K_{H_2}^{0.5} P_{H_2}^{0.5}\left(1 - \frac{p_{CH_4} p_{H_2O}^{2}}{K_{eq} p_{CO_2} p_{H_2}^{4}}\right)}{\left[1 + K_H^{0.5} P_{H_2}^{0.5} K_{HCOO} P_{CO_2} + \sqrt{K_{H_2} P_{H_2}} + K_{OH}\left(\frac{p_{H_2O}}{p_{H_2}^{0.5}}\right)\right]^2}$	51
Ni/SiO_2 (60)	260−400	1	$r_{CH_4} = \frac{k\left(p_{CO_2} p_{H_2}^{2} - \frac{p_{CH_4} p_{H_2O}^{2}}{K_{eq} p_{H_2}^{2}}\right)}{(1 + K_{H_2} p_{H_2}^{0.5} + K_{CO_2} p_{CO_2})^5}$ $r_{CH_4} = \frac{k\left(p_{CO_2} p_{H_2}^{4} - \frac{p_{CH_4} p_{H_2O}^{2}}{K_{eq}}\right)}{(1 + K_{H_2} p_{H_2}^{0.5} + K_{CO_2} p_{CO_2})^9}$	52
Ni/Cr_2O_3 (62)	160−180	1	$r_{CH_4} = k p_{CO_2}^{0.5}$	53
Ni	250−350	n.a.	$r_{CH_4} = \frac{k p_{CO_2}^{0.33} p_{H_2}}{1 + K_{H_2} p_{H_2} + K_{CO_2} p_{CO_2} + K_{H_2O} p_{H_2O}}$	54
$Ni/La_2O_3/Al_2O_3$ (17)	240−320	1	$r_{CH_4} = \frac{k p_{CO_2}^{0.33} p_{H_2}^{0.5}}{(1 + K_{H_2} p_{H_2}^{0.5} + K_{CO_2} p_{CO_2}^{0.5} + K_{H_2O} p_{H_2O})^2}$	55

https://doi.org/10.1021/acs.iecr.2c00164
Ind. Eng. Chem. Res. 2022, 61, 10419−10435

Table 1. continued

catalyst (Ni wt %)	T (°C)	P (bar)	rate equation	ref
$Ni/MgAl_2O_4$ (15)	300−400	10	$r = \frac{k_{CO_2}P_{CO_2}P_{H_2}^{0.5}\left(1 - \frac{P_{CH_4}P_{H_2O}^2}{K_{eq}P_{CO_2}P_{H_2}^4}\right)}{\left[1 + K_{H_2}P_{H_2} + K_{CO}P_{CO} + K_{CH_4}P_{CH_4} + K_{H_2O}\left(\frac{P_{H_2O}}{P_{H_2}}\right)\right]^2}$	56
Ni/Al_2O_3 (12)	180−210	1−20	$r_{CH_4} = \frac{kp_{CO_2}^{0.5}p_{H_2}^{0.5}}{(1 + K_1p_{H_2}^{0.5} + K_2p_{CO_2}^{0.5} + K_3p_{H_2O})^2}$	57
8.5% Ni/CeO_2	200−500	1−6	$r_{CH_4} = \frac{kP_{CO_2}P_{H_2}^{0.5}\left(1 - \frac{P_{CH_4}P_{H_2O}^2}{K_{eq}P_{CO_2}P_{H_2}^4}\right)}{\left(1 + K_{H_2}P_{H_2}^{0.5}\right)\left(1 + K_{CO_2}P_{CO_2} + K_{H_2O}P_{H_2O} + K_{OH}\left(\frac{P_{H_2O}}{P_{H_2}^{0.5}}\right)\right)}$	this work

of the high stability of the CO_2 molecule, which makes its activation difficult under mild conditions. In this sense, the operation under high temperature and pressure reaction conditions would increase the equipment investment as well as operational cost, which is undesirable for large-scale utilization. As a result, the development of efficient and stable catalysts is vital for CO_2 methanation.[7] Ru-, Rh-, Pt-, Pd-, Ni-, and Co-supported on metal oxides, such as Al_2O_3, CeO_2, SiO_2, ZrO_2, TiO_2, and zeolites,[8−11] are usually used as catalysts for CO_2 methanation.[12−18] Specifically, Ni/Al_2O_3 formulation is the most commercialized catalyst at the industrial level.

During the last years, Ni/CeO_2 catalyst has emerged as a promising formulation, because of an enhanced cost-to-activity ratio.[19] The high performance of this formulation is assigned to the abundant oxygen vacancies on the ceria support, enhanced metal−support interactions, and well-dispersed active metal on the ceria surface. Furthermore, it is widely accepted that CeO_2 could improve the CO_2 methanation efficiency by its participation during the CO_2 adsorption process. Chang et al.[20] have suggested that this fact contributes to inhibit the metal sites blockage by adsorbed CO_2 and, as a consequence, favors the active sites availability to perform the H_2 adsorption and CO_2 hydrogenation to methane, with respect to alumina-supported samples.

Although the catalyzed CO_2 methanation reaction has been extensively analyzed since the beginning of the 20th century, kinetic models applicable for relevant process conditions are scarce. The understanding of the reaction mechanism, including the corresponding kinetics description, is paramount in modeling, designing, and optimizing industrial operation. During the development of a kinetic model and the determination of the rate-determining step (RDS) on a specific catalyst, the use of spectroscopic techniques to gain insight on adsorbed intermediates that are formed on catalytic surface during CO_2 methanation reaction may be of great help.

Recently, much attention has been paid on determining the mechanism of CO_2 methanation over Ni- or Ru-supported catalysts.[21−24] Based on IR characterization techniques, two main reaction pathways have been proposed to describe the CO_2 hydrogenation to methane over different explored catalysts: (i) the associative adsorption of CO_2 and its hydrogenation-to-formate pathway,[25−30] and (ii) the dissociative adsorption of CO_2 in form CO*, which can be hydrogenated to formyl (CHO*) or dissociated to carbon (C*) and O*.[31] However, there is no general agreement on the reaction mechanism on Ni/CeO_2 catalyst. In this context, our own previous studies suggest the presence of two different active sites for CO_2 methanation: oxygen vacancies located at the NiO/CeO_2 interface, where CO_2 adsorption occurs, and reduced Ni sites for the dissociation of H_2.[32,33]

Taking into account the reaction pathways reported based on IR characterization techniques, different kinetic models have been proposed to describe CO_2 methanation on Ni- and Ru-based catalysts. Initially, these investigations were restricted to the determination of initial reaction rates and power-law rate equations, leading to the approach of preliminary kinetic models and apparent activation energies.[34−37] A few years later, Weatherbee et al.[38] conducted the first detailed kinetic study with a 3 wt % Ni/SiO_2 formulation operating under differential reactor conditions as well as highly diluted gas streams. From here on, many kinetic studies have been conducted over Ni- and Ru-based catalysts, using Langmuir−Hinshelwood−Hougen−Watson (LHHW) approaches. As observed in Table 1, most of the works reported have been focused on Ni-[8,39−41] and Ru-based[42−44] catalysts supported on alumina.[45−49] Although many studies have been performed, there is no consensus on the kinetic mechanism over this type of formulation, because of the different reaction conditions, reactor concept and assumptions of the rate-determining step, reaction intermediates considered and interpretation of the experimental kinetic results. Indeed, to the best of our knowledge, the kinetics of Ni/CeO_2 catalyst operating under differential and integral reactor conditions has not been attempted in the literature, since only preliminary studies under differential reactor conditions (Table 1) have been performed.[8,41] Taking into account the promising future perspectives for implementation of the Ni/CeO_2 formulation at industrial level, the aim of this work is to develop, for the first time in the literature, a kinetic model able to accurately predict the catalytic behavior of a highly active 8.5 wt % Ni/CeO_2 catalyst for CO_2 methanation under industrially relevant conditions.

With this objective, first, a set of kinetic experiments was performed under differential as well as integral reactor conditions, once the catalyst was stabilized at a temperature far from equilibrium conditions. Once a kinetic data pool was obtained and based on own mechanistic studies performed via in situ DRIFTS and isotopic experiments, as well as commonly reported reaction pathways in the literature, power-law models, as well as LHHW models, were developed, analyzed, and validated. Thus, the methodology followed in this study improves that usually reported in the literature, since we are

https://doi.org/10.1021/acs.iecr.2c00164
Ind. Eng. Chem. Res. 2022, 61, 10419−10435

proposing different kinetic models based on our prior mechanistic studies, instead of considering kinetic models derived from randomly proposed mechanism and rate-determining steps.

2. EXPERIMENTAL SECTION

2.1. Catalyst Preparation. The Ni/CeO_2 catalyst used in this study was prepared at the University of Alicante, as reported elsewhere.[32] First, CeO_2 support was obtained by calcination of cerium citrate at 600 °C for 6 h, which was previously prepared by precipitation using an ethanolic solution of $Ce(NO_3)_3{\cdot}6H_2O$ (99.5%, Alfa Aesar) and citric acid (99%, Sigma−Aldrich) in stoichiometric proportions. Then, an ethanolic solution of $Ni(NO_3)_2{\cdot}6H_2O$ (Sigma−Aldrich) was incorporated over a ceria support using the wetness impregnation method; the target Ni content was set at 9.5 wt %. Finally, the catalyst was calcined at 600 °C in static air for 6 h.

2.2. Experimental Setup. *In situ* DRIFTS experiments were performed in an infrared spectrometer (Jasco, Model FT/IR-4100) using a reaction cell for temperature and reaction gas control. The cell was designed to allow the gas flow through the catalytic bed (70 mg of undiluted catalyst). Prior to the experiments, the catalyst was pretreated with a 50% H_2/He gas mixture at 450 °C for 60 min, and then was cooled to room temperature. The background spectrum was recorded in He flow gas, and then, the methanation mixture (16% CO_2, 64% H_2 and He balance) was fed to the gas cell, raising the temperature up to 450 °C, in steps of 50 °C. Each spectrum was recorded from 4000 to 1000 cm^{-1}, with a step of 1 cm^{-1}, after keeping the sample 60 min at each temperature level.

CO_2 methanation activity, stability, and kinetic tests were performed in a cylindrical fixed-bed reactor (7 mm internal diameter) coupled to a gas chromatograph (Agilent, Model HP7890B) for measuring the outlet gas composition online. Prior to GC analysis, the water was continuously condensed in a gas/liquid separator (at −2 °C) and the resulting gas mixture was analyzed automatically, once steady state was achieved under each reaction condition. The time required to complete the outlet gas composition analysis was 12 min, which is the minimum time required to separate different compounds (H_2, N_2, CO_2, CO, and CH_4) and perform their chromatograph analysis.

Reaction experiments were performed in a 1 cm^3 catalytic bed conformed by mixing pelletized catalyst (0.3−0.5 mm) with quartz particles (0.5−0.8 mm). This represents an ∼1:1 dilution ratio and contributes to limit temperature gradients inside the catalytic bed. The temperature was continuously measured and controlled by a thermocouple placed in the middle of the catalytic bed. During activity experiments, first, the catalyst was pretreated at 500 °C for 1 h under 20% H_2/N_2 (250 cm^3 min^{-1}) flow. After cooling in pure N_2 to 200 °C, the reaction mixture was fed to the reactor with a H_2:CO_2:He molar relation of 4:1:1.25. The total flow rate was set at 250 cm^3 min^{-1}, equivalent to a space time ($W/F^{in}_{CO_2}$) of 4.67 g h mol^{-1}, with reference to a sample mass of 0.5 g, whereas the gas hour space velocity (GHSV) resulted in 15 000 h^{-1}. Once the inlet feedstream was stabilized, the catalytic behavior was explored by increasing the reaction temperature from 200 °C to 500 °C, in steps of 25 °C. Alternatively, the stability of the catalyst was evaluated by analyzing automatically the outlet feedstream, every 12 min, for 72 h on stream at 300 °C.

The activity was evaluated in terms of CO_2 conversion (X_{CO_2}), as well as selectivity toward CH_4 (S_{CH_4}) and CO (S_{CO}), which were calculated according to the following expressions:

$$X_{CO_2} = \frac{F^{in}_{CO_2} - F^{out}_{CO_2}}{F^{in}_{CO_2}} \times 100 \quad (2)$$

$$S_{CH_4}\,(\%) = \frac{F^{out}_{CH_4}}{F^{out}_{CH_4} + F^{out}_{CO}} \times 100 \quad (3)$$

$$S_{CO}\,(\%) = \frac{F^{out}_{CO}}{F^{out}_{CH_4} + F^{out}_{CO}} \times 100 \quad (4)$$

$$Y_{CH_4}\,(\%) = \frac{F^{out}_{CH_4}}{F^{in}_{CO_2}} \times 100 \quad (5)$$

$$Y_{CO}\,(\%) = \frac{F^{out}_{CO}}{F^{in}_{CO_2}} \times 100 \quad (6)$$

where $F^{in}_{CO_2}$ and $F^{out}_{CO_2}$ are the molar CO_2 flow (mol h^{-1}) at the reactor inlet and outlet, respectively. Meanwhile, F^{out}_{CO} and $F^{out}_{CH_4}$ are the molar CO and CH_4 flow (mol h^{-1}) at the reactor outlet, respectively.

Finally, the carbon balance check was performed by the following expression:

$$CB\,(\%) = \left(\frac{Y_{CH_4} + Y_{CO} + F^{out}_{CO_2}}{F^{in}_{CO_2}}\right) \times 100 \quad (7)$$

2.3. Design of Kinetic Experiments. The kinetic study was performed by the systematic variation of the operational parameters listed in Table S7 of the Supporting Information, such as reaction temperature (250−500 °C), total flow rate 200−1100 cm^3 min^{-1} (equivalent to GSHV = 12000−66000 h^{-1} or $W/F^{in}_{CO_2}$ = 1.6−24.9 g h mol^{-1}), H_2 to CO_2 ratio in the feedstream (H/C = 1−16), and total pressure (P = 1.4−6 bar). Meanwhile, N_2 was used as diluent in all experiments with the aim of minimizing the heat- and mass-transfer effect. When the water partial pressure effect is studied, a specific and controlled liquid water flow is pumped and fed as steam, after passing through an evaporator at 130 °C.

The influence of different operational parameters is evaluated working under differential (X_{CO_2} < 20%) as well as integral (X_{CO_2} > 20%) reactor conditions. For that, two different catalysts batches were used, which were composed of 0.5 and 1.0 g of Ni/CeO_2 formulation, respectively. Thus, each batch was subjected to the following experimental sequence: first, the corresponding light-off curve was obtained; second, the stability of the catalyst (72 h) was evaluated and, after that, a light-off curve was recorded; finally, the set of corresponding kinetic experiments were performed. Consequently, each catalytic batch was subjected to more than 200 h of operation.

In order to ruling out the catalyst deactivation and verifying the repeatability of the results during kinetic experiments, a reference experiment (250 or 300 °C, 2 bar and with the feed composition used during catalytic test, H_2:CO_2:N_2 molar ratio of 4:1:1.25) was systematically repeated twice per day for each catalytic batch. CO_2 conversion values were maintained at ∼14%−15% and 49−50% for the reference experiments carried

https://doi.org/10.1021/acs.iecr.2c00164
Ind. Eng. Chem. Res. 2022, 61, 10419−10435

out with the batches operating under differential (0.5 g at 250 °C) and integral (1.0 g at 300 °C) reactor conditions, respectively.

3. METHODOLOGY

3.1. Kinetic Rate Equations and Parameters Estimation. The kinetic constant was calculated using the Arrhenius law, whereas adsorption equilibrium constants (K_{H_2}, K_{CO_2}, K_{H_2O}, and K_{OH}) were estimated using the Van't Hoff expression. The correlation index between the pre-exponential factor (A_0) and activation energy (E_A) as well as adsorption enthalpies (ΔH) was minimized by parametrization, as shown in eqs 8 and 9:

$$k = k_0 \exp\left[-\frac{E_A}{R}\left(\frac{1}{T} - \frac{1}{T_{ref}}\right)\right] \tag{8}$$

$$K_i = K_{i0} \exp\left[-\frac{\Delta H}{R}\left(\frac{1}{T} - \frac{1}{T_{ref}}\right)\right] \tag{9}$$

where k and K_i are kinetic and adsorption constants at different temperatures, respectively. Meanwhile, k_0 and K_{i0} are reference constants at 350 °C (T_{ref}).

Finally, the value of equilibrium constant of CO_2 methanation reaction (K_{eq1}) was empirically estimated at every temperature as follows:[58]

$$K_{eq1} = 137T^{-3.998} \exp\left(\frac{158.7}{RT}\right) \tag{10}$$

where R is the ideal gas constant (R = 8.314 J K^{-1} mol^{-1}).

In order to estimate different kinetic parameters, a set of kinetic experiments was performed varying reactor conditions from differential (X_{CO_2} < 20%) to integral (X_{CO_2} > 20%) up to the approximation to thermodynamic equilibrium. For that, the sample mass was varied between 0.5 g and 1.0 g, respectively. Note that the partial pressures of CO_2 and H_2 keep similar along the catalytic bed for the experiments working under differential conditions. As a result, the reaction rate of CO_2 disappearance can be supposed to be the same, irrespective the position in the catalyst bed. Ultimately, the average CO_2 disappearance rate can be estimated by the following algebraic equation:

$$-\overline{r}_{CO_2} = F^{in}_{CO_2}\left(\frac{X^{out}_{CO_2} - X^{in}_{CO_2}}{W}\right) \tag{11}$$

where W is the catalyst weight (g).

However, this assumption is not valid for the experiments performed under integral reactor conditions, since the CO_2 disappearance rate ($-r_{CO_2}$) changes along the catalyst bed. Consequently, the reaction rate was determined by numerical integration of mass balance equation established for the plug-flow reactor model:

$$\frac{W}{F^{in}_{CO_2}} = \int_0^{X^{out}_{CO_2}} \frac{dX_{CO_2}}{-r_{CO_2}} = \int_0^{X^{out}_{CO_2}} \frac{dX_{CO_2}}{f(T, X_{CO_2})} \tag{12}$$

3.2. Computational Methods. A nonlinear regression analysis was performed to estimate kinetic parameters by minimizing the sum of the squares of the differences between experimental and calculated variable (y) for each point of the entire set of kinetics experiments (N). Note that y variable was considered in the form of reaction rate (eq 11) or CO_2 conversion (integrated eq 12):

$$SSE = \sigma^2 = \sum_i^N (y^{exp} - y^{calc})^2 \tag{13}$$

The fitting and estimation of different kinetic parameters was performed by *lsqcurvefit* and *fminsearch* commands of MATLAB software (R2014b version). The former is a nonlinear least-squares solver. In contrast, the *fminsearch* command performs a nonlinear multidimensional minimization without restrictions by the Nelder–Mead algorithm with the following optimization options: a tolerance function (TolFun) of 10^{-10}, lower bound of step size (TolX) of 10^{-3}, and a maximum of 500 interactions (iter).

The *Ode23* command was used for the numerical integration of eq 12, which solves nonstiff differential equation systems by adaptative Runge–Kutta algorithm of second and third order.

Finally, the model discrimination was performed by comparing the absolute mean deviation parameters, which were determined by the following expression:

$$D(\%) = \sqrt{\frac{\sigma^2}{N}}\frac{1}{\overline{y}} \times 100 \tag{14}$$

where $\overline{y}$ is the mean value of the experimental variable.

4. RESULTS

4.1. Catalyst Characterization. Ni/CeO_2 catalyst was deeply characterized in our previous work.[32] Briefly, the catalyst presents CeO_2 (JCPDS No. 00-034-0394) and NiO (JCPDS No. 01-075-0269) as crystal phases, a Ni content of 8.5 wt % and a specific surface area of 15 m^2 g^{-1}. Regarding redox properties, the sample shows a small sharp peak at 250 °C, with small shoulders at lower temperature that can be assigned to NiO reduction. Furthermore, it also shows a large peak at 345 °C with a shoulder at higher temperature, which is assigned to the simultaneous reduction of NiO and surface CeO_2 in close contact. Moreover, a third peak is observed at 810 °C related to the reduction of bulk ceria.

The variation of nickel and ceria oxidation state during the CO_2 methanation reaction was studied by XPS. For that, the Ni 2p and Ce 3d energy regions were analyzed for this catalyst before and after the activity experiments. On the one hand, Ni 2p region shows a single peak for the prereduced Ni/CeO_2 catalyst centered at 854.8 eV. Note that this position evidence a shift of more than 1 eV, with respect to the peak position of conventional Ni/Al_2O_3 catalyst, evidencing a different NiO–support interaction. Furthermore, a shoulder at lower binding energy (852.2 eV) was identified, which indicated the presence of Ni^0. This distribution of nickel species, combining Ni^{2+} and Ni^0, is maintained after the catalytic tests.[31] On the other hand, the analysis of Ce 3d spectrum denotes the presence of Ce^{4+} and Ce^{3+} before/after the catalytic test. Finally, the joint analysis of O 1s and C 1s spectra suggests that carbon species are removed from the catalyst surface during reaction. Thus, the presence of two different Ni sites is noted by XPS analysis; namely, reduced nickel suitable for H_2 dissociation and cationic nickel, probably stabilized in the NiO/ceria interface, is involved in the CO_2 dissociation.

The presence of different active sites was further supported by the study of CO_2 methanation mechanism by isotopic

https://doi.org/10.1021/acs.iecr.2c00164
Ind. Eng. Chem. Res. 2022, 61, 10419−10435

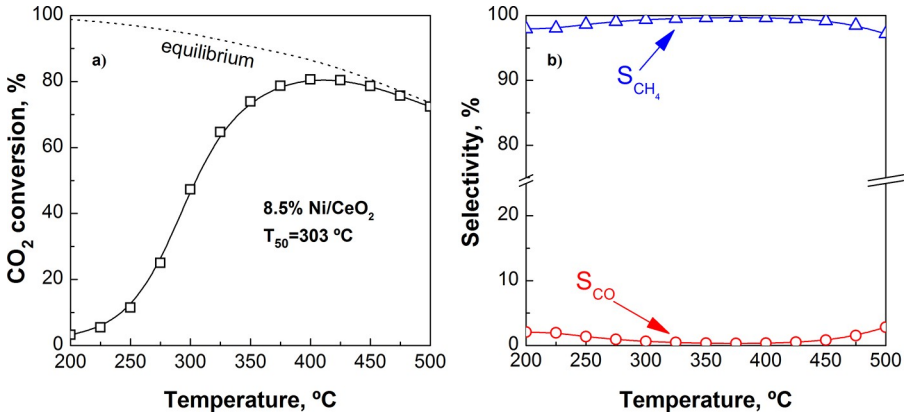

Figure 1. (a) Light-off curve and (b) selectivity toward CH_4 (S_{CH_4}) and CO (S_{CO}) of Ni/CeO_2 catalyst recorded prior to the stability test.

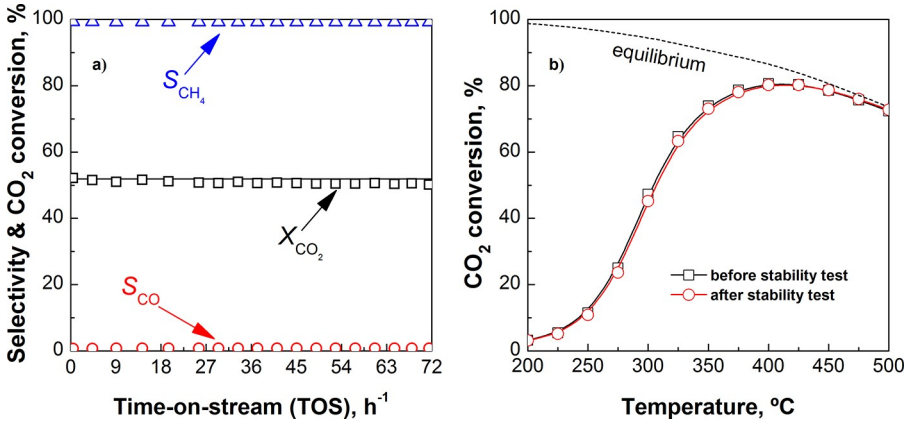

Figure 2. (a) CO_2 conversion as well as selectivity toward CH_4 (S_{CH_4}) and CO (S_{CO}) during stability test at 300 °C and (b) light-off curves before/after stability testing.

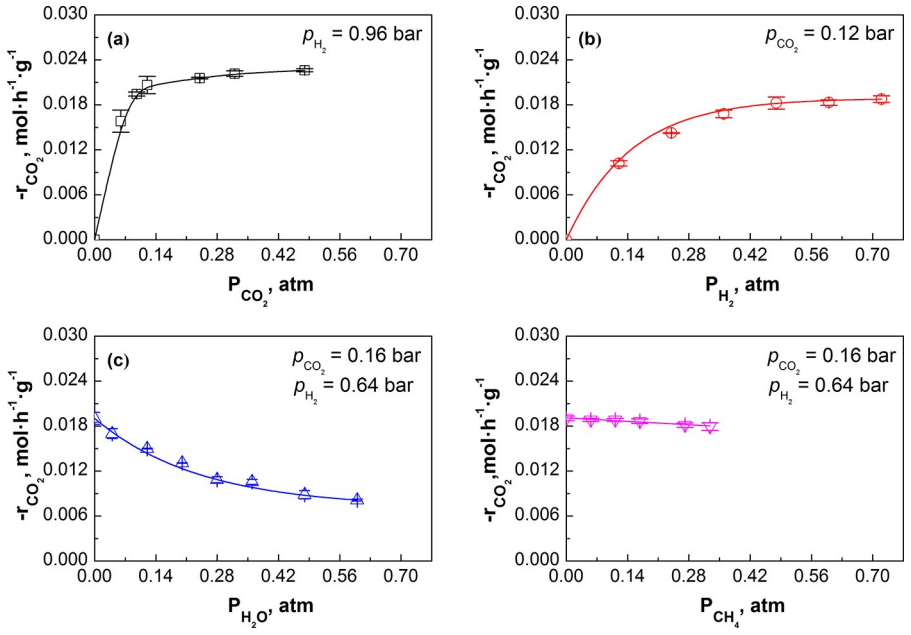

Figure 3. Influence of: (a) CO_2 (p_{CO_2}), (b) H_2 (p_{H_2}), (c) H_2O (p_{H_2O}), and (d) CH_4 (p_{CH_4}) partial pressures on CO_2 methanation rate at 275 °C. Total pressure of 2 bar and GHSV = 15 000 h^{-1}.

experiments. Pulse experiments denote that slow H_2O formation and fast CO_2 chemisorption do not necessarily occur on the same active sites, which is consistent with the possible participation of NiO/CeO_2 interface in the latter. In fact, the detection of ^{16}O in all oxygen-containing species (i.e., $^{13}C^{16}O_2$), supplied from the catalyst, also suggests that the high

https://doi.org/10.1021/acs.iecr.2c00164
Ind. Eng. Chem. Res. 2022, 61, 10419−10435

oxygen and vacant mobility of ceria support favors oxygen exchange between the catalyst and CO_2 molecules.

4.2. Activity and Stability Test. The CO_2 conversion (X_{CO_2}) curve, as well as the selectivity toward methane (S_{CH_4}) and carbon monoxide (S_{CO}) of Ni/CeO_2 catalyst, as a function of temperature, are included in Figures 1a and 1b, respectively.

The Ni/CeO_2 catalyst shows a maximum X_{CO_2} of ~80% at 375−400 °C with a S_{CH_4} above 95% in the entire temperature range. Indeed, the temperature required to achieve a CO_2 conversion of 50% (T_{50}) is 303 °C. Thus, these results confirm the high activity and selectivity of the Ni/CeO_2 catalyst in CO_2 methanation reaction, which makes it even more suitable to perform the kinetic study. Based on our own previous studies, the high CO_2 methanation performance is related to the presence of two different actives sites for CO_2 dissociation (NiO/ceria interface) and for H_2 dissociation (reduced Ni^0 particles), the limited water adsorption on CO_2 adsorption sites and a faster chemisorption of CO_2.[31,32]

Catalyst stability was checked under reactive conditions (stoichiometric composition of the reactant mixture) during a long-term (72 h) CO_2 methanation experiment at 300 °C (Figure 2a). As can be observed, the CO_2 conversion decreases slightly, from 52% to 50% during stability test, whereas the selectivity toward CH_4 and CO remains invariable near 100% and 0%, respectively. Indeed, no relevant changes were observed in the evolution of X_{CO_2} with temperature for the experiments performed before/after stability test (Figure 2b). In agreement with the similar XRD patterns (Figure S1 of the Supporting Information) and the average Ni^0 crystallites sizes (Table S1 of the Supporting Information), Ni particles sintering during kinetic experiments can be discarded and, consequently, the activity of the Ni/CeO_2 catalyst has been stabilized. Thus, it can be considered that the catalyst activity remains unchanged during the entire set of kinetic experiments under extended variable conditions.

4.3. Kinetic Measurements. As observed in Table S7, during the set of kinetic experiments, CH_4 and minor amounts of CO were the only products detected by GC, whereas the carbon balance closed within ±5%.

4.3.1. Effect of Reagents and Products Partial Pressure. Figure 3 shows the impact of the inlet mixture composition on the CO_2 hydrogenation rate for the experiments conducted under a total pressure of 2 bar, a total flow rate of 500 cm^3 min^{-1}, and a temperature of 275 °C. In these experiments, the CO_2 disappearance rate can be calculated using eq 11, since CO_2 conversion is <20% (differential conditions).

The effects of H_2/CO_2 inlet ratio on the CO_2 hydrogenation rate was investigated either at constant CO_2 partial pressure (p_{CO_2} = 0.12) or H_2 partial pressure (p_{H_2} = 0.96). A saturating tendency can be observed when increasing p_{CO_2} from 0 to 0.48 bar (Figure 3a). Indeed, two differentiated zones can be identified: <0.14 bar, where $-r_{CO_2}$ rises significantly, and >0.14 bar, where it remains almost constant. As reported by Weatherbee et al.,[38] CO_2 hydrogenation is strongly affected by CO_2 concentration at low partial pressures, whereas is almost insensitive at higher pressures. Similar positive effect can be observed on $-r_{CO_2}$ when p_{H_2} increases from 0 to 0.72 bar at constant p_{CO_2} (Figure 3b). Specifically, the $-r_{CO_2}$ value increases up to an H_2 partial pressure of 0.49 bar, and then it is stabilized at ~0.018 mol h^{-1} g^{-1}. In agreement with Weatherbee et al.[38] and Van Herwijnen et al.,[50] a positive apparent order for both reagents can be identified at low pressures, while the reaction is approaching zero order at higher partial pressures. In order to analyze the influence of each reagent on CO_2 reaction rate, the reported data were fitted to a simple power-law expression by logarithmic linearization and multiple linear regression:

$$-r_{CO_2} = k p_{CO_2}^{\alpha} p_{H_2}^{\beta} \tag{15}$$

where k is the kinetic constant at 275 °C, whereas α and β are the CO_2 and H_2 apparent reaction orders, respectively.

The apparent reaction orders for CO_2 and H_2 resulted in 0.06 and 0.29, respectively. Thus, the hydrogen has a stronger influence on the CO_2 reaction rate. This behavior is consistent with that reported in the literature,[39,59] denoting that H_2 feed content plays a fundamental role on both CO_2 adsorbed species dissociation and the removal of OH^- adsorbed species at the surface.[44]

Figures 3c and 3d show the influence of H_2O (p_{H_2O}) and CH_4 (p_{CH_4}) addition in the feed stream on the CO_2 hydrogenation rate ($-r_{CO_2}$) at constant CO_2 (0.16 bar) and H_2 (0.64 bar) partial pressures. An inhibition effect of H_2O partial pressure on $-r_{CO_2}$ is detected when it increases from 0 to 0.49 bar, whereas no influence of CH_4 partial pressure (p_{CH_4}) is detected. This fact denotes that the kinetic constant is affected by the concentration of adsorbed water or hydroxyls (OH^-), which ultimately denotes a competitive adsorption of these compounds and reagents on same active sites. As a result, eq 15 should be modified as follows in order to reflect such water resistance:[48]

$$-r_{CO_2} = \frac{k p_{CO_2}^{\alpha} p_{H_2}^{\beta}}{1 + K_{H_2O} p_{H_2O}} \tag{16}$$

where K_{H_2O} is the water adsorption constant at 275 °C.

In order to linearize eq 16, a plot of $1/-r_{CO_2}$ vs p_{H_2O} was made and fitted to experimental reaction rates. Then, the kinetic and water adsorption constants were estimated from the intercept and the slope of the regression line, which results in 0.0089 mol h^{-1} g^{-1} $bar^{-0.35}$ and 3.635 bar^{-1}, respectively. The validity of these parameters is supported by their positive sign and similar values to others reported in the literature.[49]

Finally, the effect of inert partial pressure was also analyzed. For that, increasing total flow rates were tested for a specific CO_2 and H_2 flow rates (see Figure S2 in the Supporting Information). As expected, as the inert gas fraction increases from 100 to 800 cm^3 min^{-1} (GSHV of 15 000−60 000 h^{-1}), the CO_2 hydrogenation rate slightly decreases, especially at lower total flow rates.

4.3.2. Effect of the Reaction Temperature. Figure 4 presents the impact of the reaction temperature (250−295 °C) on CO_2 conversion at different space times ($W/F_{CO_2}^{in}$). Experimental points show that X_{CO_2} increases with temperature, because of the promotion of the kinetic constant with the temperature, according to the Arrhenius equation. Since X_{CO_2} follows a saturating tendency toward the equilibrium (X_{eq}), the initial reaction rates approach was chosen to calculate apparent kinetic constants. First, experimental points

https://doi.org/10.1021/acs.iecr.2c00164
Ind. Eng. Chem. Res. 2022, 61, 10419−10435

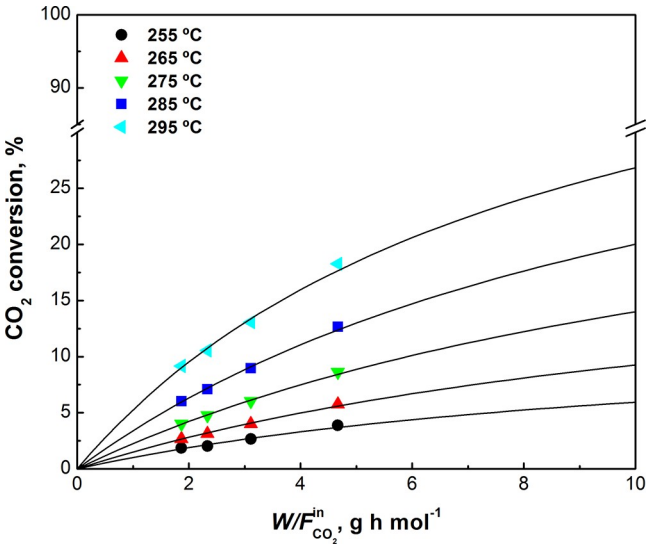

Figure 4. Effect of temperature on CO_2 conversion at increasing space times ($W/F^{in}_{CO_2}$). Symbols refer to experimental data and black lines to the obtained fits. Total pressure of 2 bar and H_2/CO_2 ratio of 4 in the feedstream.

were fitted (black lines) to the following mathematical expression, with a and b as fitting coefficients:

$$-r_{CO_2} = \frac{(W/F^{in}_{CO_2})^b}{a + \frac{(W/F^{in}_{CO_2})^b}{X_{eq}}} \quad (17)$$

The derivative of eq 17 at $W/F^{in}_{CO_2} = 0$ allowed to calculate the initial reaction rates ($-r^0_{CO_2}$) at different temperatures:

$$-r^0_{CO_2} = \left(\frac{dX_{CO_2}}{d(W/F^{in}_{CO_2})}\right)_{W/F^{in}_{CO_2}=0} = k_{ap} f(C^{in}_{CO_2}, C^{in}_{H_2}) \quad (18)$$

Then, considering the logarithmic Arrhenius expression, the apparent activation energy is determined from the slope of graphic representation of $\ln(-r^0_{CO_2})$ vs $1/T$ (Figure 5):

$$\ln(-r^0_{CO_2}) = \ln[A_0 f(C^0_{CO_2}, C^0_{H_2})] - \frac{E_{ap}}{R}\left(\frac{1}{T}\right) \quad (19)$$

The apparent activation energy for the CO_2 methanation reaction on Ni/CeO_2 catalyst resulted in 103.9 kJ mol^{-1}. As observed in Table S2 in the Supporting Information, this value is consistent with others reported in the literature for CO_2 methanation on different catalysts; e.g., values in the range of 75−118 kJ mol^{-1} and 53.5−113 kJ mol^{-1} have been reported for Ni/Al_2O_3-type[39,45,47,48,60,61] and Ni/CeO_2[8,41,62−65] catalysts, respectively.

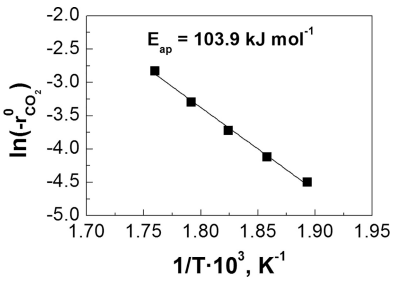

Figure 5. Arrhenius plot and the corresponding apparent activation energy obtained from the results reported in Figure 4.

In order to confirm the validity of determined apparent activation energies, Mears[66] and Anderson[67] criteria were checked under the most unfavorable operational conditions (see the Supporting Information). Dimensionless values below 0.15 and 0.75 were obtained, which indicates that intraparticle and external heat- and mass-transfer limitations can be ruled out under reported operational conditions.

4.3.3. Effect of Total Pressure. The effect of pressure on the process kinetics was tested in the range of 2−6 bar at 350 °C. Figure 6 shows the evolution of CO_2 conversion with increasing space times ($W/F^{in}_{CO_2}$) at 2, 4, and 6 bar. As expected, CO_2 conversion is boosted by raising the system pressure, which is consistent with the volume contraction derived from the Sabatier reaction stoichiometry. Specifically, the improvement is ∼10% when the pressure increases from 2 bar to 6 bar. However, the improvement in CO_2 conversion is partially limited due to the operation near to thermodynamic equilibrium at this temperature (350 °C).

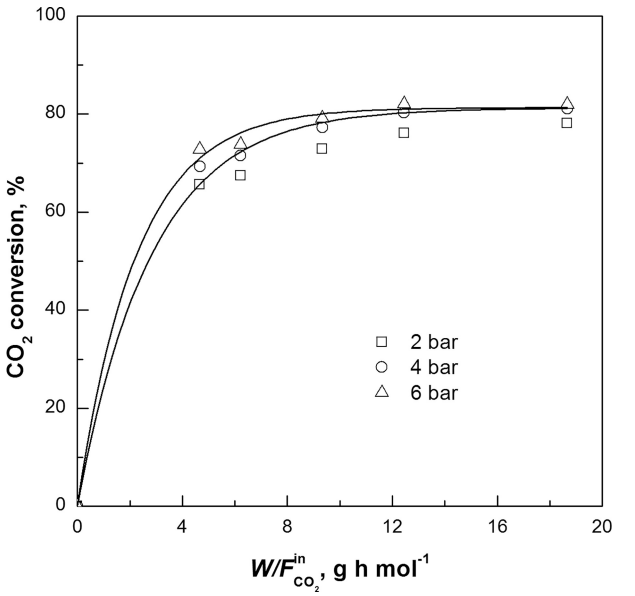

Figure 6. Effect of space time ($W/F^{in}_{CO_2}$) on CO_2 conversion at different pressures. [Conditions: H_2/CO_2 ratio of 4 in the feedstream and a reaction temperature of 350 °C.]

4.4. Kinetic Modeling. The validity of different rate expressions for CO_2 methanation obtained for the commonly reported reaction mechanisms is investigated in this section. For that, following LHHW approaches, each reaction path is considered as an elementary step and the slowest step (rate-determining step, RDS) should be identified for the determination of kinetic expressions. All other elementary steps are assumed to be in quasi-equilibrium or irreversible.

As previously introduced, it is widely accepted that CO_2 methanation can occur via direct CO_2 adsorption and hydrogenation (associative mechanism) or via previous CO_2 dissociation (dissociative mechanism), respectively. In the former, CO_2 conversion to methane can occur via carbonate or formate (COOH*) as the reaction intermediates,[8,27,29] where-

https://doi.org/10.1021/acs.iecr.2c00164
Ind. Eng. Chem. Res. 2022, 61, 10419−10435

as CO_2 is adsorbed in the form of CO* in the latter, which can be further dissociated to carbon (C*) or hydrogenated to formyl (CHO*), respectively. An alternative route, based on CO formation through formate decomposition, has also been reported. However, the absence of carbonyl species during DRIFTS experiments discards this mechanistic route for the Ni/CeO_2 catalyst.[68] In order to clarify the real reaction pathway, three commonly accepted reaction mechanisms are summarized in Tables 2, 3, and 4. As can be observed, at least 9 mechanistic equations can be proposed for each catalytic route by varying the RDS among different adsorption, reaction, or desorption elementary steps. However, based on the knowledge gained in our previous mechanistic[11,31,32] and kinetic studies,[69] we were able to select the most probable rate-determining step for each reaction mechanism more specifically.

Finally, note that the effect of RWGS reaction in the kinetic model has been neglected, since the CO amount produced in the set of kinetic experiments is almost negligible. Indeed, the selectivity toward this compound is <2% for all recorded kinetic data (Table S7); contrary to that observed in our previous kinetic study with a Ni/Al_2O_3 catalyst, where CO selectivities of >30% were reported and, consequently, the effect of RWGS reaction should have been considered to improve the model accuracy.[69]

4.4.1. Dissociative Formyl Mechanism. This mechanism has been proposed recently by Koschany et al.[45] for a coprecipitated $NiAl(O)_x$ catalyst. As outlined in Table 2, this

Table 2. Elementary Steps of Dissociative Formyl Mechanism

step	reaction	assumption
1	$H_2 + 2* \rightleftarrows 2H*$	quasi equilibrium
2	$CO_2 + 2* \rightleftarrows CO* + O*$	quasi-equilibrium
3	$CO* \rightleftarrows CO(g) + *$	quasi-equilibrium
4	$CO* + H* \rightleftarrows CHO* + *$	rate-determining step
5	$CHO* + * \rightleftarrows CH + *O*$	low CHO* coverage
6	$CH* + 3H* \rightleftarrows CH_4* + 3*$	low CH_x* coverage
7	$CH_4* \rightleftarrows CH_4(g) + *$	low CH_4* coverage
8	$O* + H* \rightleftarrows OH* + *$	low O* coverage
9	$OH* + H* \rightleftarrows H_2O* + *$	quasi-equilibrium
10	$H_2O* \rightleftarrows H_2O(g) + *$	low H_2O* coverage

reaction pathway assumes the dissociative adsorption of H_2 and CO_2 in form of hydrogen atoms (H*) and carbonyls (CO*) on a Ni^0 surface, respectively.[70] Then, CO* reacts with H*, forming carbon-hydroxyl (COH*) or adsorbed formyl (CHO*, step 4 in Table 2). After that, an additional carbon−oxygen bond cleavage occurs yielding carbenes (CH_x*, step 5 in Table 2). Finally, this species is further hydrogenated to form methane (step 7 in Table 2). Concurrently, the reaction between the adsorbed oxygen and H atom leads to the formation of hydroxyls, which are further hydrogenated to form H_2O (steps 8 and 9 in Table 2). Note that the desorption of carbonyls in the form CO_{gas} cannot be ruled out, instead of being hydrogenated (step 3 in Table 2). Step 4 in Table 2 was considered as the rate-determining step (RDS), since the hydrogenation of carbonyl (CO*) is usually quite slow.[45−47] As a consequence, the previous steps as well as step 9 in Table 2 are assumed to be at quasi-equilibrium, whereas the remaining steps are kinetically irrelevant, because of the low coverage of reaction intermediates (extremely fast steps).[46,59]

Taking into account these considerations, the following rate equation of CO_2 methanation is deduced (see the Supporting Information):

$$-r_{CO_2} = \frac{kP_{CO_2}^{0.5}P_{H_2}^{0.5}\left(1 - \frac{P_{CH_4}P_{H_2O}^2}{K_{eq}P_{CO_2}P_{H_2}^4}\right)}{\left[1 + K_{C_x}P_{CO_2}^{0.5} + K_{H_2}P_{H_2}^{0.5} + K_{H_2O}P_{H_2O} + K_{OH}\left(\frac{P_{H_2O}}{P_{H_2}^{0.5}}\right)\right]^2} \quad (20)$$

where k is the apparent kinetic constant, whereas K_{H_2} and K_{H_2O} are the hydrogen and water adsorption constants, whereas K_{C_x} and $K_{OH}K_{OH}$ are the lumped constants of the adsorbed carbon and hydroxyl surface intermediates.

4.4.2. Dissociative Carbon Mechanism. This reaction pathway was proposed by Dalmon and Martin for Ni/SiO_2 catalysts.[71] As reported in formyl mechanism, dissociative adsorption of H_2 and CO_2 occurs in this reaction pathway, leading to hydrogen atoms (H*) and carbonyls (CO*) formation on Ni^0 surface[70] (see Table 3), respectively.

Table 3. Elementary Steps of Dissociative Carbon Mechanism

step	reaction	assumption
1	$H_2 + 2* \rightleftarrows 2H*$	quasi equilibrium
2	$CO_2 + 2* \rightleftarrows CO* + O*$	quasi-equilibrium
3	$CO* \rightleftarrows CO(g) + *$	quasi-equilibrium
4	$CO* + * \rightleftarrows C* + O*$	rate-determining step
5	$C* + H* \rightleftarrows *CH + *$	low C* coverage
6	$CH* + 3H* \rightleftarrows CH_4* + 3*$	low CH_x* coverage
7	$CH_4* \rightleftarrows CH_4(g) + *$	low CH_4* coverage
8	$O* + H* \rightleftarrows OH* + *$	low O* coverage
9	$OH* + H* \rightleftarrows H_2O* + *$	quasi-equilibrium
10	$H_2O* \rightleftarrows H_2O(g) + *$	low H_2O* coverage

However, carbonyls are further dissociated to carbon (C*) and O* (C, step 4 in Table 3) in this case. Then, these species are hydrogenated to carbenes (CH_x*, step 5 in Table 3) and hydroxyls (step 8 in Table 3), intermediate compounds that are finally hydrogenated into methane (step 6 in Table 3) and water (step 9 in Table 3), respectively. Furthermore, some of the adsorbed carbonyls can be desorbed as CO_{gas} instead of being hydrogenated (step 3 in Table 3).

The kinetic rate equation obtained was derived, assuming that the dissociation of carbonyl (step 4 in Table 3) is quite slow and, consequently, is considered the RDS.[38] As in formyl mechanism, we assume that steps 1−3 and 9 in Table 3 are at quasi-equilibrium, whereas we consider that the rest of steps are kinetically irrelevant, because of the low coverage of reaction intermediates (extremely fast steps).[46,59] As a result, the following rate equation of CO_2 methanation is derived (see the Supporting Information):

$$-r_{CO_2} = \frac{kP_{CO_2}^{0.5}P_{H_2}^{0.25}\left(1 - \frac{P_{CH_4}P_{H_2O}^2}{K_{eq}P_{CO_2}P_{H_2}^4}\right)}{\left[1 + K_{C_x}P_{CO_2}^{0.5}P_{H_2}^{0.25} + K_{H_2}P_{H_2}^{0.5} + K_{H_2O}P_{H_2O} + K_{OH}\left(\frac{P_{H_2O}}{P_{H_2}^{0.5}}\right)\right]^2} \quad (21)$$

where k is the apparent kinetic constant and K_{H_2} and K_{H_2O} are the hydrogen and water adsorption constants, whereas K_{C_x} and

https://doi.org/10.1021/acs.iecr.2c00164
Ind. Eng. Chem. Res. 2022, 61, 10419−10435

K_{OH} are the lumped constants of the adsorbed carbon and hydroxyl surface intermediates.

4.4.3. Associative Formate Mechanism. This kinetic mechanism was first reported by Ibraeva et al.[72] on a commercial nickel−alumina−calcium catalyst. Contrary to the previously reported for carbon and formyl mechanisms, CO_2 is molecularly chemisorbed, preferentially in form of bicarbonates (HCO_3*) on OH^- groups of the support at the surface), as observed in Table 4. Then, the adsorbed

Table 4. Elementary Steps of Associative Formate Mechanism

step	reaction	assumption
1	$H_2 + 2* \rightleftarrows 2H*$	quasi equilibrium
2	$CO_2 + * \rightleftarrows CO_2*$	quasi-equilibrium
3	$CO_2* + H* \rightleftarrows HCOO* + *$	rate-determining step
4	$HCOO* + H* \rightleftarrows CHO + *OH*$	low HCOO* coverage
5	$CHO* + H* \rightleftarrows CH* + OH*$	low CHO* coverage
6	$CH* + 3H* \rightleftarrows CH_4* + 3*$	low CH_x* coverage
7	$CH_4* \rightleftarrows CH_4(g) + *$	low CH_4* coverage
8	$OH* + H* \rightleftarrows H_2O* + *$	quasi-equilibrium
9	$H_2O* \rightleftarrows H_2O(g) + *$	low H_2O* coverage

bicarbonates can be easily hydrogenated to formate species (HCOO*, step 3 in Table 4) by H adsorbed on near metal particles with H atoms migrating from the surface of Ni particles.[44] Then, formats are decomposed into hydroxyls (OH*) and formyls (CHO*) in a H-assisted pathway (step 4 in Table 4).[8] Finally, the formyl formed is sequentially reduced up to CH_4 (steps 5 and 6 in Table 4). Simultaneously, hydroxyls (OH*) are hydrogenated to form water.

In this case, step 3 in Table 4 has been considered as the RDS, considering steps 1, 2, and 9 in quasi-equilibrium; meanwhile, the rest of the steps are kinetically irrelevant, because of the low coverage of reaction intermediates (extremely fast steps).[46,59] Taking into account these considerations, the rate equation of CO_2 methanation can be expressed as follows (see the Supporting Information):

$$-r_{CO_2} = \frac{kP_{CO_2}P_{H_2}^{0.5}\left(1 - \frac{P_{CH_4}P_{H_2O}^{2}}{K_{eq}P_{CO_2}P_{H_2}^{4}}\right)}{\left[1 + K_{CO_2}P_{CO_2} + K_{H_2}P_{H_2}^{0.5} + K_{H_2O}P_{H_2O} + K_{OH}\left(\frac{P_{H_2O}}{P_{H_2}^{0.5}}\right)\right]^2} \quad (22)$$

where k is the apparent kinetic constant and K_{H_2}, K_{CO_2}, and K_{H_2O} are the hydrogen, carbon dioxide, and water adsorption constants, whereas K_{OH} is a lumped adsorption constant of the adsorbed hydroxyl surface intermediates.

4.5. Model Discrimination. Once previous kinetic models were developed, the corresponding CO_2 hydrogenation rates were determined by combining numerical integration of eq 12 and nonlinear regression analysis. As already explained in Section 3.1, the kinetic constants, as well as the adsorption constants, were determined according to the Arrhenius (eq 8) and Van't Hoff (eq 9) expressions, respectively. Meanwhile, the equilibrium constant of CO_2 methanation reaction (K_{eq1}) was estimated using eq 10. On the other hand, the reagents and products partial pressures were estimated by eqs S72−S76 in the Supporting Information). In order to determine the kinetic and adsorption parameters with more certainty, all kinetic measurements reported in Table S7 were employed. Finally, a comparison of the variance (eq 13) and mean absolute deviation (eq 14) values is used for model discrimination, as introduced in Section 3.2.

Figure 7 includes the parity plots of the formyl, carbonyl, and formate kinetic models. With regard to the formyl model

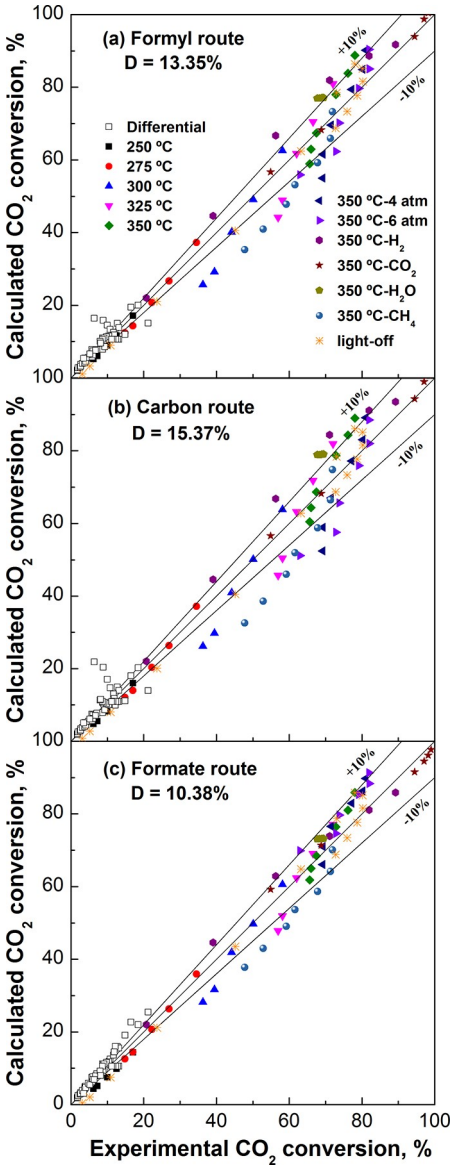

Figure 7. Parity plots of (a) formyl, (b) carbon, and (c) formate models adjusted to experimental data obtained operating with differential as well as integral reactor conditions. Hollow black squares (□) correspond to data obtained under differential reactor conditions.

(Figure 7a), this mechanism considers the dissociative CO_2 adsorption, leading to CO formation, which finally is hydrogenated to formyl (RDS). This alternative achieves a mean absolute residual of 13.35% (σ^2 = 0.3304). In fact, many points were outside the ±10% dispersion region. This LHHW model systematically overestimates CO_2 conversion under differential reaction conditions (X_{CO_2} < 20%). Meanwhile, it underestimates the effect of methane (350 °C−CH_4) and overestimates the effect of H_2 (350 °C−H_2) and water (350 °C−H_2O) under integral reactor conditions (X_{CO_2} > 20%).

https://doi.org/10.1021/acs.iecr.2c00164
Ind. Eng. Chem. Res. 2022, 61, 10419−10435

The carbon route (Figure 7b), which considers a dissociative CO formation mechanism, being the dissociation of carbonyl (CO*) as RDS, shows a mean absolute residual of 15.37% (σ^2 = 0.4375). Although this model has been widely accepted for describing kinetics on highly loaded (>15 wt %) Ni/Al_2O_3 and $NiAl(O)_x$ formulations,[45−48] it should be discarded for our Ni/CeO_2 catalyst, since it shows lower statistical significance than the formyl model. The inferior fit of this model could be mainly related to the different Ni-support interaction derived from the specific properties of ceria support, such as basic sites concentration, excellent redox properties, and high oxygen vacancies concentration. Furthermore, differences in the Ni loading, oxidation state, and distribution alter the way that CO_2 is adsorbed onto the catalyst.[73] As a result, fewer points are within the ±10% dispersion region. A remarkable overestimation of CO_2 conversion under differential reactor conditions can be noticed, as well as poorer estimation of CO_2 conversion under integral reactor conditions (X_{CO_2} > 20%). Specifically, the main deviations are observed for the dataset corresponding to the effect of methane (350 °C−CH_4) and hydrogen partial pressures (350 °C−H_2).

Finally, the parity plot shown in Figure 7c denotes that the formate model, which consists of the associative CO_2 adsorption and assumes its hydrogenation to formate as RDS, presented an outstanding ability for describing the experimental CO_2 conversion data. In fact, this model shows the lowest mean absolute deviation (10.38%) and variance (σ^2 = 0.1933). As a result, the majority of points are within the ±10% dispersion region. However, the effect of methane admission in the feed stream operating under integral reactor conditions is not so well predicted. Furthermore, the model also has a tendency to overestimate CO_2 conversion under differential reactor conditions. Anyway, the obtained decrease in the absolute mean residual compared with respect to carbonyl and formyl alternatives clearly suggests that hydrogen and monodentate or bidentate carbonates, formed due to CO_2 associative adsorption, rather than CO formed through CO_2 dissociative adsorption, are directly hydrogenated to formate during CO_2 methanation over Ni/CeO_2 catalysts, as previously suggested by other authors based on IR mechanistic studies.[8,25,74]

4.6. Formate on Two Active Sites Model Validation and Parameter Estimation. As observed in the previous section, the formate model, in which the hydrogenation of adsorbed CO_2 to formate is considered to be the RDS, shows a fitting quality statistically more significant than that of formyl and carbon models. Note that the hydrogenation and dissociation of adsorbed CO formed due to CO_2 dissociative adsorption were considered the RDS for formyl and carbonyl models, respectively. In order to validate the reaction mechanism proposed by the formate model (Table 4), *in situ* DRIFTS experiments were performed. Figure 8 plots the spectra recorded at increasing temperatures after the exposition of the sample to CO_2 methanation feedstream during 60 min. Note that the background spectra recorded at room temperature in He has been subtracted for all spectra. On the one hand, an intense double band at ∼2350 cm^{-1} (not shown) is detected, which belongs to gas-phase CO_2. On the other hand, O−H stretching of bicarbonates created due to the CO_2 reaction with surface hydroxyl groups is also observed above 3500 cm^{-1}; meanwhile, the bands identified below 1700 cm^{-1}, which are ascribed to the presence of monodentate and bidentate carbonates, formed due to CO_2 reaction with surface oxygen species, are identified.[15,31,32,75,76]

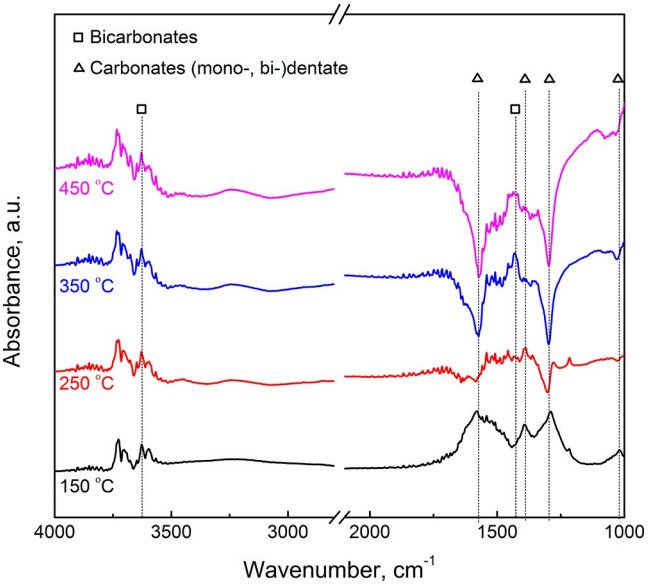

Figure 8. *In situ* DRIFTS spectra recorded under 16% CO_2/64% H_2/He reaction stream at 150, 250, 350, and 450 °C for 8.5% Ni/CeO_2 catalyst.

Note that bands belonging to monodentate and bidentate carbonates are only detected in the spectrum at 150 °C. Above this temperature, these bands disappear with a simultaneous formation of negative bands. In contrast, the bands ascribed to bicarbonates (1430 and 3625 cm^{-1}) remain invariable with reaction temperature, because of their higher stability. This trend denotes that carbonates adsorbed on the catalyst surface are easily removed when the methanation reaction is activated (Figure 2). Meanwhile, bicarbonates are more stable and, as consequence, can be considered as the most abundant reaction intermediates (MARI) in CO_2 methanation over Ni/CeO_2 catalyst. Indeed, it is generally reckoned that formates are originated from the reaction of bicarbonate species with dissociated hydrogen.[25,75,77,78] Thus, the high amount of bicarbonates detected seems to be in accordance with the assumption considering the hydrogenation of associatively adsorbed CO_2 to formate as the RDS. Moreover, the absence of DRIFT absorption bands assigned to adsorbed carbonyl species discards the CO_2 methanation through a CO intermediate,[68,74,79] as it happens in formyl and carbon intermediate mechanisms. This fact is consistent with the less-statistical significance of these models, where the dissociation and hydrogenation of CO, formed due to CO_2 dissociation, are considered as the RDS, respectively.

In summary, the best fitting of formate model is in good agreement with the *in situ* DRIFT results obtained during CO_2 methanation reaction. Nevertheless, our own studies, as well as previous studies reported in the literature, suggest that the CO_2 methanation reaction over Ni/CeO_2 catalyst occurs on two different active sites. On the one hand, CO_2 is adsorbed and activated on ceria sites, more specifically in oxygen vacancies near to NiO−CeO_2 interface. On the other hand, H_2 adsorption and subsequent dissociation into H atoms occurs on Ni^0 sites. Then, these H atoms rapidly diffuse to near CO_2 adsorption sites via a spillover process.[29,32,33,74] Thus, the presence of two different active sites sould not be neglected

https://doi.org/10.1021/acs.iecr.2c00164
Ind. Eng. Chem. Res. 2022, 61, 10419−10435

when deducing the rate equation by LHHW approaches. In order to further improve the intrinsic kinetic description of CO_2 methanation on Ni/CeO_2 catalysts, the following rate equation was deduced (see the Supporting Information), assuming the hydrogenation of adsorbed CO_2 to formate as the RDS (see Table 5):

$$r_{CH_4} = \frac{kP_{CO_2}P_{H_2}^{0.5}\left(1 - \frac{P_{CH_4}P_{H_2O}^{2}}{K_{eq}P_{CO_2}P_{H_2}^{4}}\right)}{(1 + K_{H_2}P_{H_2}^{0.5})\left[1 + K_{CO_2}P_{CO_2} + K_{H_2O}P_{H_2O} + K_{OH}\left(\frac{P_{H_2O}}{P_{H_2}^{0.5}}\right)\right]} \quad (23)$$

Table 5. Elementary Steps of Associative Formate Mechanism on Two Active Sites[a]

step	reaction	assumption
1	$H_2 + 2^* \rightleftarrows 2H^*$	quasi-equilibrium
2	$CO_2 + \hat{} \rightleftarrows \hat{CO_2}$	quasi-equilibrium
3	$CO_2\hat{} + H^* \rightleftarrows HCOO\hat{} + *$	rate-determining step
4	$HCOO\hat{} + H^* \rightleftarrows CHO\hat{} + OH^*$	low HCOO^ coverage
5	$CHO\hat{} + H^* \rightleftarrows CH\hat{} + OH^*$	low CHO^ coverage
6	$CH\hat{} + 3H^* \rightleftarrows CH_4\hat{} + 3^*$	low CH_x^ coverage
7	$CH_4\hat{} \rightleftarrows CH_4(g) + \hat{}$	low CH_4^ coverage
8	$OH^* + H^* \rightleftarrows H_2O^* + *$	quasi-equilibrium
9	$H_2O^* \rightleftarrows H_2O(g) + *$	low H_2O* coverage

[a]Asterisk symbol (*) refers to Ni^0 sites for H_2 dissociation. Circumflex symbol (^) refers to CO_2 adsorption sites near to Ni-CeO_2 interface.

where k is an apparent kinetic constant and K_{H_2}, K_{CO_2}, and K_{H_2O} are the hydrogen, carbon dioxide, and water adsorption constants, whereas K_{OH} is a lumped adsorption constant of the adsorbed hydroxyl surface intermediates adsorbed. As can be observed, the adsorption constants are coincident with that reported for the formate model on a single active site (eq 22), which suggest that the same intermediates (the most abundant reaction intermediates (MARI)) slow the reaction rate. The main difference lies in the denominator of the equation, where two terms appear because of the presence of two different active sites.

Figure 9 shows the corresponding parity plot to formate model on two different active sites. The prediction accuracy of the model was similar to that above observed for formate mechanism on a single active site (Figure 7c). Specifically, the mean deviation value is 11.26%. However, not systematic deviation of CO_2 conversion is obtained under analyzed operational conditions. Thus, the kinetic equation is able to describe with high statistical significance the effect of temperature, pressure as well as H_2/CO_2 molar ratio over the extended range of conditions employed. As can be observed, the model well accounts the effect of the different operational parameters on CO_2 conversion when the system operates under differential reactor conditions (empty black squares). Indeed, lower deviations can be noticed with respect to formate model on a single site. Furthermore, most points are within the ±10% region in the high-activity region (X_{CO_2} > 20%), which denotes that the model predicts with high accuracy the promoting effect of reagents and the system total pressure on reaction kinetic as well as the inhibiting effect of water and the insensitivity to p_{CH_4} at 350 °C. Therefore, no systematic underestimation of CO_2 conversion for the

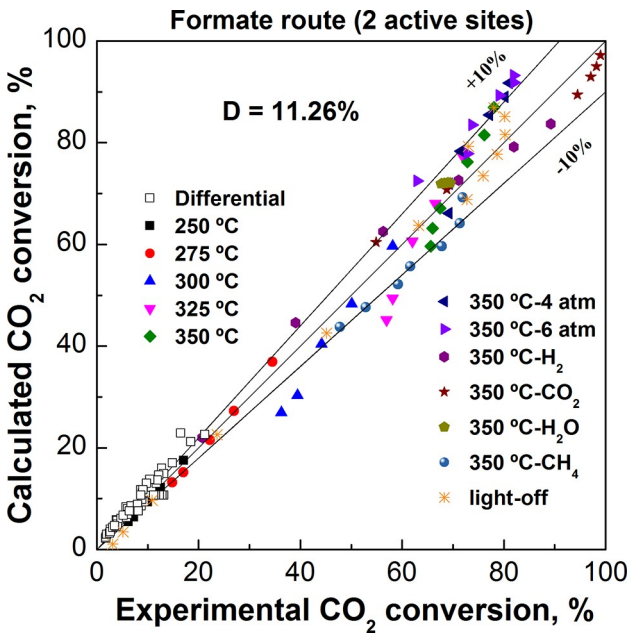

Figure 9. Parity plot of two active sites-based formate model adjusted to experimental data obtained operating with differential as well as integral reactor conditions. Hollow black squares (□) correspond to data obtained under differential reactor conditions.

experiments performed at increasing CH_4 partial pressures; in contrast to the observed for formate model on a single active site (Figure 7c). The lower prediction quality is obtained when the system is working under kinetically controlled regime (300 and 325 °C) at low space times ($W/F^{in}_{CO_2}$). As a consequence, these results reflect the satisfactory prediction of CO_2 conversion under integral reactor conditions, which is a region of great interest for the industrial application.

Finally, adsorption constants and enthalpies has been determined combining numerical integration of eq 12 and nonlinear regression. The estimated constants for the chosen mechanistic model are summarized in Table 6 at different

Table 6. Kinetic as Well as Adsorption Constants Estimated at Different Temperatures for the Formate Route on Two Different Active Sites

		Adsorption Constants			
temp, T (°C)	apparent kinetic constant, k (mol g^{-1} h^{-1} $bar^{-1.5}$)	K_{H_2O} (bar^{-1})	K_{OH} ($bar^{-0.5}$)	K_{CO_2} (bar^{-1})	K_{H_2}($bar^{-0.5}$)
250	1.23	0.44	17.76	36.97	1.65
300	3.62	0.37	11.51	20.80	1.12
350	8.97	0.32	7.99	12.84	0.81
400	19.43	0.29	5.86	8.51	0.61
450	37.82	0.26	4.48	5.97	0.48

temperatures. In order to evaluate the quality of the parameters and the model, the 95% confidence intervals and the covariance, as well as the correlation (or anticorrelation) matrix, were determined at the reference temperature (350 °C), as shown in Tables S4−S6 of the Supporting Information. All reported constants show narrow confident intervals (Table S4), which indicates the individual statistical relevance of all kinetic parameters. Furthermore, moderate to weak correlations (or anticorrelations) have been found for all kinetic

https://doi.org/10.1021/acs.iecr.2c00164
Ind. Eng. Chem. Res. 2022, 61, 10419−10435

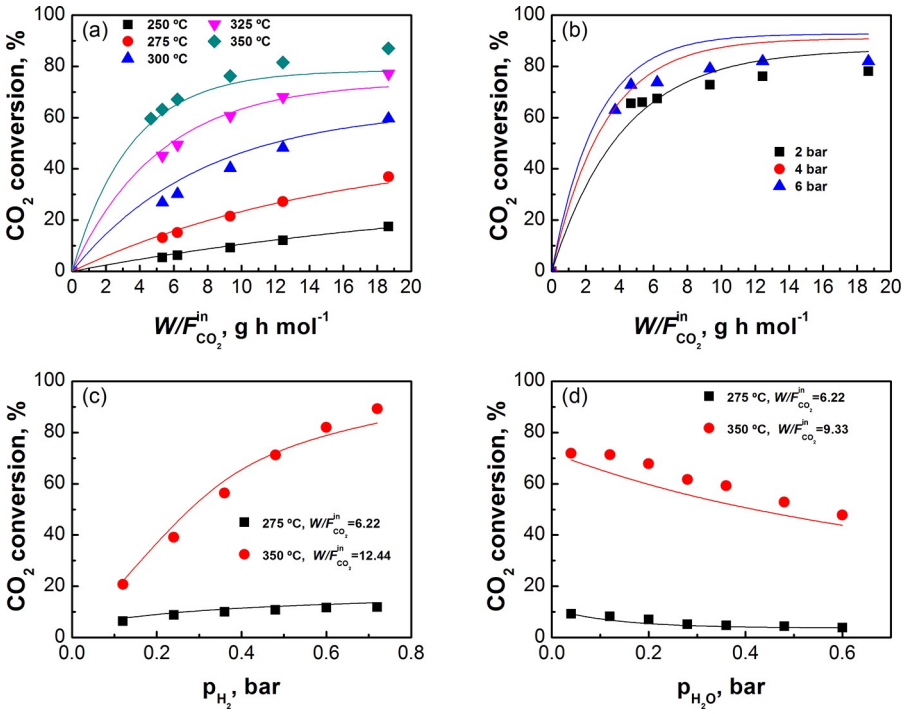

Figure 10. Comparison of experimental (points) and predicted (lines) CO_2 conversion values as a function of (a) reaction temperature at increasing space times (2 bar), (b) system total pressure, and (c) H_2 and (d) H_2O partial pressures at two temperatures and space times.

parameters reported, which validates the validity of all kinetic parameters here proposed.[51]

From a mechanistic point of view, all resulting final parameters are physically more realistic and present more consistent values than those obtained by the formate route based on a single active site (not included), which increases the validity of the mechanistic model proposed here. The apparent kinetic constant of CO_2 methanation rate increases progressively from 1.23 mol g^{-1} h^{-1} $bar^{-1.5}$ (250 °C) to 37.82 mol g^{-1} h^{-1} $bar^{-1.5}$ (450 °C). On the other hand, relative higher values are obtained for the adsorption constants. This fact suggests that reaction rates are clearly influenced by adsorbed reaction intermediates except H_2O, which presents significantly lower values. Specifically, the adsorption constants of OH^- and, especially, of CO_2 are at least 1 order of magnitude higher than that of hydrogen. Thus, adsorbed bicarbonates and hydroxyls have higher inhibiting effect on CO_2 methanation than water or hydrogen, which is consistent with the most abundant reaction intermediates (MARI) on the surface of the catalyst identified by *in situ* DRIFT study (Figure 8). Finally, the value of the apparent activation energy for CO_2 hydrogenation (53.9 kJ mol^{-1}) is similar to that reported for similar Ni/CeO_2 catalyst.[41]

Note that all adsorption constants fulfill the strong criteria established by Boudart et al.,[80] whereas adsorption enthalpies (eq 12) present values of −19.4, − 21.6, − 8.3 and −28.7 kJ mol^{-1} for hydrogen (ΔH_{H_2}), hydroxyls (ΔH_{OH}), water (ΔH_{H_2O}), and CO_2 (ΔH_{CO_2}) adsorption, respectively. According to Boudart rules, a negative value of the entropy variation of an adsorption process ($\Delta S < 0$) is indicative of a more-ordered state, and should be within the following range:

$$10 < \Delta S < 12.2 - 0.0014\Delta H \tag{24}$$

This parameter has been determined by combining the Van't Hoff expression and the Gibbs function ($\Delta G^\circ = \Delta H^\circ - T\Delta S^\circ$), as follows:

$$\ln(K) = -\frac{\Delta H^\circ}{RT} + \frac{\Delta S^\circ}{R}; \qquad \Delta S^\circ = R\ln(K) + \frac{\Delta H^\circ}{T} \tag{25}$$

Hydrogen, hydroxyls, water, and CO_2 adsorption entropies result in values of −33.0, −17.5, −22.8, and −24.8 J mol^{-1}, respectively. Noteworthy, the lowest entropies correspond to hydroxyl and water adsorption, which suggests less stable species, as reported in our previous work.[32] Note that hydrogen presents an entropy value 10−16 J mol^{-1} higher than the rest of the compounds, confirming its key role in the CO_2 methanation rate, as deduced from results included in Figure 3.

The validity of the model was further analyzed comparing experimental (points) versus predicted (lines) CO_2 conversion values at different reaction conditions (Figure 10). As can be observed in Figure 10, the model predicts well the positive effect of (a) increasing temperature, (b) system pressure, and (c) H_2/CO_2 ratio, on CO_2 conversion. Furthermore, the inhibitory effect of water (Figure 10d) is also well-predicted. Taking into account that the water content at the reactor outlet would be notable, the accurate prediction of the inhibiting effect of water is critical for the industrial scale application.

Finally, the experimental and predicted light-off curves were compared (Figure 11). Note that the experimental points were obtained with the same feed composition reported in Figures 1 and 2. As can be observed, the kinetic model based on formate route on two different active sites accurately predicts CO_2 conversion values, irrespective the reaction temperature, further validating the kinetic model here proposed. In accordance with the parity plots, the main deviations are observed at CO_2 conversion values near the equilibrium

https://doi.org/10.1021/acs.iecr.2c00164
Ind. Eng. Chem. Res. 2022, 61, 10419−10435

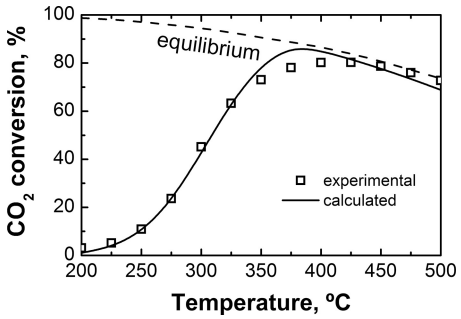

Figure 11. Comparison of experimental light-off curve (points) and predicted one (line) for a feed composition of 16% of CO_2, 64% of H_2 and 20% of N_2, and a total pressure of 1.4 bar.

conversion (~350 °C); in particular, the model predicts a faster approach to thermodynamic equilibrium.

In summary, the formate mechanistic model, which assumes two different active sites, is able to describe, with high accuracy, the intrinsic kinetics of CO_2 methanation over 8.5 wt % Ni/CeO_2 catalyst under a wide range of operational conditions. It has provided a high fitting quality to the experimental kinetic data (124 runs) and kinetic parameters realistic physical significance. To the best of the authors' knowledge, these results represent the first complete intrinsic kinetic study reported in the literature for a highly active Ni/CeO_2 catalyst.

5. CONCLUSIONS

A dataset composed of 124 experimental points has been collected and analyzed with the aim of developing a kinetic model able to reflect the intrinsic kinetic of the 8.5 wt % Ni/CeO_2 catalyst in CO_2 methanation reaction. Different kinetic expressions of the reaction rate, developed through LHHW approach, were fitted to experimental data with that aim. The best fit of experimental data was obtained with formate LHHW mechanistic model assuming the hydrogenation of bicarbonates to formate as the rate-determining step (RDS). This model can predict satisfactorily the positive effect of the increasing reagents partial pressure (p_{CO_2} and p_{H_2}), the reaction temperature, the system pressure, and the H_2/CO_2 molar ratio in the feedstream on the CO_2 methanation reaction from differential (X_{CO_2} < 20%) to equilibrium (X_{CO_2} > 80%) reactor conditions. Furthermore, the detrimental effect of strongly adsorbed OH^- and H_2O surface intermediates on catalytic activity is well-predicted. In fact, the mean absolute deviation (D = 10.38%) of this model is significantly lower than the obtained (D > 13.35%) for other common models explored in the literature, in which the conversion of CO_2 to carbonyl (CO_{ads}) occurs (such as carbon and formyl routes), for the description of the kinetics of Ni/Al_2O_3-type catalysts during CO_2 methanation. Finally, in the consideration of a kinetic model, two different active sites for CO_2 adsorption (Ni/CeO_2 interface) and H_2 dissociation (Ni^0) also provide an accurate prediction (D = 11.26%) of the intrinsic kinetics of CO_2 methanation on Ni/CeO_2 catalyst. Although the mean deviation value obtained is slightly higher than that obtained for the formate model on a single active site, the obtained kinetic parameters are physically more realistic, which further validates this alternative model. According to this mechanism, Ni and Ce sites present an active role in CO_2 methanation on Ni/CeO_2 catalysts, so enhancing the interaction between metal and support is critical to enhance CO_2 methanation over this promising formulation and should be a focus of study in the near future. For the first time in the literature, this work provides a LHHW-type mechanism capable of accurately reflecting the kinetics of CO_2 methanation reaction on Ni/CeO_2 catalyst with high accuracy under a broad range of operating conditions. This kinetic expression can be employed for the design of a full-scale methanation reactor.

■ ASSOCIATED CONTENT

Supporting Information

The Supporting Information is available free of charge at https://pubs.acs.org/doi/10.1021/acs.iecr.2c00164.

Characterization of fresh and used samples (XRD results and Ni crystallite sites), influence of GHSV on CO_2 methanation rate and an overview of kinetics models and apparent activation energies presented in the literature. Furthermore, assessment of mass and heat-transfer limitations, statistical validation of the kinetic model, derivation of LHHW kinetic rate equations and operational conditions and data pool of kinetic experiments (PDF)

■ AUTHOR INFORMATION

Corresponding Author

Juan R. González-Velasco − *Department of Chemical Engineering, Faculty of Science and Technology, University of the Basque Country UPV/EHU, 48940 Leioa, Bizkaia, Spain*; orcid.org/0000-0002-8679-1805; Email: juanra.gonzalezvelasco@ehu.eus

Authors

Jon A. Onrubia-Calvo − *Department of Chemical Engineering, Faculty of Science and Technology, University of the Basque Country UPV/EHU, 48940 Leioa, Bizkaia, Spain*

Adrián Quindimil − *Department of Chemical Engineering, Faculty of Science and Technology, University of the Basque Country UPV/EHU, 48940 Leioa, Bizkaia, Spain*

Arantxa Davó-Quiñonero − *Department of Inorganic Chemistry, University of Alicante, 03080 Alicante, Spain*

Alejandro Bermejo-López − *Department of Chemical Engineering, Faculty of Science and Technology, University of the Basque Country UPV/EHU, 48940 Leioa, Bizkaia, Spain*

Esther Bailón-García − *Department of Inorganic Chemistry, University of Alicante, 03080 Alicante, Spain*

Beñat Pereda-Ayo − *Department of Chemical Engineering, Faculty of Science and Technology, University of the Basque Country UPV/EHU, 48940 Leioa, Bizkaia, Spain*

Dolores Lozano-Castelló − *Department of Inorganic Chemistry, University of Alicante, 03080 Alicante, Spain*

José A. González-Marcos − *Department of Chemical Engineering, Faculty of Science and Technology, University of the Basque Country UPV/EHU, 48940 Leioa, Bizkaia, Spain*; orcid.org/0000-0002-5962-7938

Agustín Bueno-López − *Department of Inorganic Chemistry, University of Alicante, 03080 Alicante, Spain*; orcid.org/0000-0002-5434-6459

Complete contact information is available at: https://pubs.acs.org/10.1021/acs.iecr.2c00164

Author Contributions

J.A.O.-C. was responsbile for the conceptualization, data curation, investigation, methodology, validation. visualization, writing (original draft). A.Q. was responsible for conceptualization, data curation, methodology, visualization, and writing (review and editing). A.D.-Q. was responsible for methodology (catalyst synthesis and characterization), and writing (review and editing). A. Bermejo-López was responsible for data curation, methodology, visualization, review (editing). E.B.-G. was responsible methodology (catalyst synthesis and characterization) and writing (review and editing). B.P.-A. was responsible for conceptualization, data curation, methodology, visualization, review, and editing. D.L.-C. was responsible for funding adquisition, validation, and writing (review and editing). J.A.G.-M. was responsible for funding acquisition, formal analysis, resources, and software. A. Bueno-López was responsible for funding acquisition, validation, and writing (review and editing). J.R.G.-V. was responsible for conceptualization, funding acquisition, project administration, resources, supervision, and writing (review and editing).

Notes

The authors declare no competing financial interest.

■ ACKNOWLEDGMENTS

Support for this study was provided by the Spanish Ministry of Science and Innovation (Project Nos. PID2019-105960RB-C21 and PID2019-105960RB-C22) and the Basque Government (Project No. IT1297-19). J.A.O.-C. acknowledges the Postdoctoral research grant (No. DOCREC20/49) provided by the University of the Basque Country. A.Q. also acknowledges University of the Basque Country for his Ph.D. grant (No. PIF-15/351).

■ REFERENCES

(1) Rau, G. H.; Baird, J. R. Negative-CO_2-emissions ocean thermal energy conversion. *Renew. Sust. Energy Rev.* **2018**, *95*, 265.
(2) Gervais, F. Anthropogenic CO_2 warming challenged by 60-yearcycle. *Earth-Sci. Rev.* **2016**, *155*, 129.
(3) Child, M.; Koskinen, O.; Linnanen, L.; Breyer, C. Sustainability guardrails for energy scenarios of the global energy transition. *Renewable Sustianable Energy Rev.* **2018**, *91*, 321.
(4) Zhang, X.; Bauer, C.; Mutel, C. L.; Volkart, K. Life cycle assessment of power-to-gas: Approaches, system variations and their environmental implications. *Appl. Energy* **2017**, *190*, 326.
(5) Sabatier, P. New synthesis of methane. *Comptes Rendus* **1902**, *134*, 514.
(6) Gao, J.; Wang, Y.; Ping, Y.; Hu, D.; Xu, G.; Gu, F.; Su, F. A thermodynamic analysis of methanation reactions of carbon oxides for the production of synthetic natural gas. *RSC Adv.* **2012**, *2* (6), 2358.
(7) Li, W.; Wang, H.; Jiang, X.; Zhu, J.; Liu, Z.; Guo, X.; Song, C. A short review of recent advances in CO_2 hydrogenation to hydrocarbons over heterogeneous catalysts. *RSC Adv.* **2018**, *8* (14), 7651.
(8) Bian, Z.; Chan, Y. M.; Yu, Y.; Kawi, S. Morphology dependence of catalytic properties of Ni/CeO_2 for CO_2 methanation: A kinetic and mechanism study. *Catal. Today* **2020**, *347*, 31.
(9) Le, T. A.; Kim, T. W.; Lee, S. H.; Park, E. D. Effects of Na content in Na/Ni/SiO_2 and Na/Ni/CeO_2 catalysts for CO and CO_2 methanation. *Catal. Today* **2018**, *303*, 159.
(10) Tan, J.; Wang, J.; Zhang, Z.; Ma, Z.; Wang, L.; Liu, Y. Highly dispersed and stable Ni nanoparticles confined by MgO on ZrO_2 for CO_2 methanation. *Appl. Surf. Sci.* **2019**, *481*, 1538.
(11) Quindimil, A.; De-La-Torre, U.; Pereda-Ayo, B.; González-Marcos, J. A.; González-Velasco, J. R. Ni catalysts with la as promoter supported over Y- and BETA- zeolites for CO_2 methanation. *Appl. Catal., B* **2018**, *238*, 393.
(12) Alrafei, B.; Polaert, I.; Ledoux, A.; Azzolina-Jury, F. Remarkably stable and efficient Ni and Ni-Co catalysts for CO_2 methanation. *Catal. Today* **2020**, *346*, 23.
(13) Bermejo-López, A.; Pereda-Ayo, B.; González-Marcos, J. A.; González-Velasco, J. R. Mechanism of the CO_2 storage and in situ hydrogenation to CH_4. Temperature and adsorbent loading effects over Ru-CaO/Al_2O_3 and Ru-Na_2CO_3/Al_2O_3 catalysts. *Appl. Catal., B* **2019**, *256*, 117845.
(14) Bermejo-López, A.; Pereda-Ayo, B.; González-Marcos, J. A.; González-Velasco, J. R. Ni loading effects on dual function materials for capture and in-situ conversion of CO_2 to CH_4 using CaO or Na_2CO_3. *J. CO_2 Util.* **2019**, *34*, 576.
(15) Karelovic, A.; Ruiz, P. Mechanistic study of low temperature CO_2 methanation over Rh/TiO_2 catalysts. *J. Catal.* **2013**, *301*, 141.
(16) Mihet, M.; Lazar, M. D. Methanation of CO_2 on Ni/γ-Al_2O_3: Influence of Pt, Pd or Rh promotion. *Catal. Today* **2018**, *306*, 294.
(17) Nguyen, H. T. T.; Kumabe, Y.; Ueda, S.; Kan, K.; Ohtani, M.; Kobiro, K. Highly durable Ru catalysts supported on CeO_2 nanocomposites for CO_2 methanation. *Appl. Catal., A* **2019**, *577*, 35.
(18) Shin, H. H.; Lu, L.; Yang, Z.; Kiely, C. J.; McIntosh, S. Cobalt catalysts decorated with platinum atoms supported on barium zirconate provide enhanced activity and selectivity for CO_2 methanation. *ACS Catal.* **2016**, *6* (5), 2811.
(19) Alcalde-Santiago, V.; Davó-Quiñonero, A.; Lozano-Castelló, D.; Quindimil, A.; De-La-Torre, U.; Pereda-Ayo, B.; González-Marcos, J. A.; González-Velasco, J. R.; Bueno-López, A. Ni/LnOx catalysts (Ln = La, Ce or Pr) for CO_2 methanation. *ChemCatChem.* **2018**, *11* (2), 810.
(20) Chang, K.; Zhang, H.; Cheng, M.; Lu, Q. Application of ceria in CO_2 conversion catalysis. *ACS Catal.* **2020**, *10* (1), 613.
(21) Panagiotopoulou, P.; Verykios, X. E. Mechanistic study of the selective methanation of CO over Ru/TiO_2 catalysts: Effect of metal crystallite size on the nature of active surface species and reaction pathways. *J. Phys. Chem. C* **2017**, *121* (9), 5058.
(22) Petala, A.; Panagiotopoulou, P. Methanation of CO_2 over alkali-promoted Ru/TiO_2 catalysts: I. effect of alkali additives on catalytic activity and selectivity. *Appl. Catal., B* **2018**, *224*, 919.
(23) Zhou, G.; Liu, H.; Cui, K.; Xie, H.; Jiao, Z.; Zhang, G.; Xiong, K.; Zheng, X. Methanation of carbon dioxide over Ni/CeO_2 catalysts: Effects of support CeO_2 structure. *Int. J. Hydrogen Energy* **2017**, *42* (25), 16108.
(24) Kim, A.; Debecker, D. P.; Devred, F.; Dubois, V.; Sanchez, C.; Sassoye, C. CO_2 methanation on Ru/TiO_2 catalysts: On the effect of mixing anatase and rutile TiO_2 supports. *Appl. Catal., B* **2018**, *220*, 615.
(25) Lee, S. M.; Lee, Y. H.; Moon, D. H.; Ahn, J. Y.; Nguyen, D. D.; Chang, S. W.; Kim, S. S. Reaction mechanism and catalytic impact of Ni/CeO_{2-x} catalyst for low-temperature CO_2 methanation. *Ind. Eng. Chem. Res.* **2019**, *58* (20), 8656.
(26) Guo, X.; He, H.; Traitangwong, A.; Gong, M.; Meeyoo, V.; Li, P.; Li, C.; Peng, Z.; Zhang, S. Ceria imparts superior low temperature activity to nickel catalysts for CO_2 methanation. *Catal. Sci. Technol.* **2019**, *9* (20), 5636.
(27) Pan, Q.; Peng, J.; Wang, S.; Wang, S. In situ FTIR spectroscopic study of the CO_2 methanation mechanism on Ni/$Ce_{0.5}Zr_{0.5}O_2$. *Catal. Sci. Technol.* **2014**, *4* (2), 502.
(28) Zhou, G.; Liu, H.; Cui, K.; Jia, A.; Hu, G.; Jiao, Z.; Liu, Y.; Zhang, X. Role of surface Ni and Ce species of Ni/CeO_2 catalyst in CO_2 methanation. *Appl. Surf. Sci.* **2016**, *383*, 248.
(29) Ye, R.-P.; Li, Q.; Gong, W.; Wang, T.; Razink, J. J.; Lin, L.; Qin, Y.-Y.; Zhou, Z.; Adidharma, H.; Tang, J.; et al. High-performance of nanostructured Ni/CeO_2 catalyst on CO_2 methanation. *Appl. Catal., B* **2020**, *268*, 118474.
(30) Zhang, J.; Yang, Y.; Liu, J.; Xiong, B. Mechanistic understanding of CO_2 hydrogenation to methane over Ni/CeO_2 catalyst. *Appl. Surf. Sci.* **2021**, *558*, 149866.
(31) Cárdenas-Arenas, A.; Quindimil, A.; Davó-Quiñonero, A.; Bailón-García, E.; Lozano-Castelló, D.; De-La-Torre, U.; Pereda-Ayo, B.; González-Marcos, J. A.; González-Velasco, J. R.; Bueno-López, A.

Isotopic and in situ DRIFTS study of the CO_2 methanation mechanism using Ni/CeO_2 and Ni/Al_2O_3 catalysts. *Appl. Catal., B* **2020**, *265*, 118538.
(32) Cárdenas-Arenas, A.; Quindimil, A.; Davó-Quiñonero, A.; Bailón-García, E.; Lozano-Castelló, D.; De-La-Torre, U.; Pereda-Ayo, B.; González-Marcos, J. A.; González-Velasco, J. R.; Bueno-López, A. Design of active sites in Ni/CeO_2 catalysts for the methanation of CO_2: Tailoring the $Ni\text{-}CeO_2$ contact. *Appl. Mater. Today* **2020**, *19*, 100591.
(33) Cárdenas-Arenas, A.; Cortés, H. S.; Bailón-García, E.; Davó-Quiñonero, A.; Lozano-Castelló, D.; Bueno-López, A. Active, selective and stable $NiO\text{-}CeO_2$ nanoparticles for CO_2 methanation. *Fuel Process. Technol.* **2021**, *212*, 106637.
(34) Chiang, J. H.; Hopper, J. R. Kinetics of the hydrogenation of carbon dioxide over supported nickel. *Ind. Eng. Chem. Prod. Res. Dev.* **1983**, *22* (2), 225.
(35) Hayes, R. E.; Thomas, W. J.; Hayes, K. E. A study of the nickel-catalyzed methanation reaction. *J. Catal.* **1985**, *92* (2), 312.
(36) Lunde, P. J.; Kester, F. L. Carbon dioxide methanation on a ruthenium catalyst. *Ind. Eng. Chem. Prod. Des. Dev.* **1974**, *13* (1), 27.
(37) Dew, J. N.; White, R. R.; Sliepcevich, C. M. Hydrogenation of carbon dioxide on nickel-kieselguhr catalyst. *Ind. Eng. Chem.* **1955**, *47* (1), 140.
(38) Weatherbee, G. D.; Bartholomew, C. H. Hydrogenation of CO_2 on group VIII metals: II. kinetics and mechanism of CO_2 hydrogenation on nickel. *J. Catal.* **1982**, *77* (2), 460.
(39) Lefebvre, J.; Bajohr, S.; Kolb, T. A comparison of two-phase and three-phase CO_2 methanation reaction kinetics. *Fuel* **2019**, *239*, 896.
(40) Loder, A.; Siebenhofer, M.; Lux, S. The reaction kinetics of CO_2 methanation on a bifunctional Ni/MgO catalyst. *J. Ind. Eng. Chem.* **2020**, *85*, 196.
(41) Yu, Y.; Chan, Y. M.; Bian, Z.; Song, F.; Wang, J.; Zhong, Q.; Kawi, S. Enhanced performance and selectivity of CO_2 methanation over $g\text{-}C_3N_4$ assisted synthesis of $NiCeO_2$ catalyst: Kinetics and DRIFTS studies. *Int. J. Hydrogen Energy* **2018**, *43* (32), 15191.
(42) Duyar, M. S.; Ramachandran, A.; Wang, C.; Farrauto, R. J. Kinetics of CO_2 methanation over $Ru/\gamma\text{-}Al_2O_3$ and implications for renewable energy storage applications. *J. CO_2 Util.* **2015**, *12*, 27.
(43) Falbo, L.; Visconti, C. G.; Lietti, L.; Szanyi, J. The effect of CO on CO_2 methanation over Ru/Al_2O_3 catalysts: A combined steady-state reactivity and transient DRIFT spectroscopy study. *Appl. Catal., B* **2019**, *256*, 117791.
(44) Wang, X.; Hong, Y.; Shi, H.; Szanyi, J. Kinetic modeling and transient DRIFTS−MS studies of CO_2 methanation over Ru/Al_2O_3 catalysts. *J. Catal.* **2016**, *343*, 185.
(45) Koschany, F.; Schlereth, D.; Hinrichsen, O. On the kinetics of the methanation of carbon dioxide on coprecipitated NiAl(O)x. *Appl. Catal., B* **2016**, *181*, 504.
(46) Burger, T.; Donaubauer, P.; Hinrichsen, O. On the kinetics of the co-methanation of CO and CO_2 on a co-precipitated Ni-Al catalyst. *Appl. Catal., B* **2021**, *282*, 119408.
(47) Miguel, C. V.; Mendes, A.; Madeira, L. M. Intrinsic kinetics of CO_2 methanation over an industrial nickel-based catalyst. *J. CO_2 Util.* **2018**, *25*, 128.
(48) Marocco, P.; Morosanu, E. A.; Giglio, E.; Ferrero, D.; Mebrahtu, C.; Lanzini, A.; Abate, S.; Bensaid, S.; Perathoner, S.; Santarelli, M.; Pirone, R.; Centi, G. CO_2 methanation over Ni/Al hydrotalcite-derived catalyst: Experimental characterization and kinetic study. *Fuel* **2018**, *225*, 230.
(49) Champon, I.; Bengaouer, A.; Chaise, A.; Thomas, S.; Roger, A. Carbon dioxide methanation kinetic model on a commercial Ni/Al_2O_3 catalyst. *J. CO_2 Util.* **2019**, *34*, 256.
(50) Van Herwijnen, T.; Van Doesburg, H.; De Jong, W. A. Kinetics of the methanation of CO and CO_2 on a nickel catalyst. *J. Catal.* **1973**, *28* (3), 391.
(51) Hernandez Lalinde, J. A.; Roongruangsree, P.; Ilsemann, J.; Bäumer, M.; Kopyscinski, J. CO_2 methanation and reverse water gas shift reaction. Kinetic study based on in situ spatially-resolved measurements. *Chem. Eng. J.* **2020**, *390*, 124629.
(52) Binder, G. G.; White, R. R. Synthesis of Methane from Carbon Dioxide and Hydrogen. *Chem. Eng. Prog.* **1950**, *46*, 563−574.
(53) Solc, M. Kinetik der Hydrierung des Kohlendioxyds zu Methan an einem Nickel-Chrom(III)-oxyd-Katalysator. *Collect. Czech. Chem. C* **1962**, *27*, 2621.
(54) Inoue, H.; Funakoshi, M. Kinetics of methanation of carbon monoxide and carbon dioxide. *J. Chem. Eng. Jpn.* **1984**, *17* (6), 602.
(55) Kai, T.; Takahashi, T.; Furusaki, S. Kinetics of the methanation of carbon dioxide over a supported $Ni\text{-}La_2O_3$ catalyst. *Can. J. Chem. Eng.* **1988**, *66* (2), 343.
(56) Xu, J.; Froment, G. F. Methane steam reforming, methanation and water-gas shift: I. intrinsic kinetics. *AIChE J.* **1989**, *35* (1), 88.
(57) Yang Lim, J.; McGregor, J.; Sederman, A. J.; Dennis, J. S. Kinetic studies of CO_2 methanation over a $Ni/\gamma\text{-}Al_2O_3$ catalyst using a batch reactor. *Chem. Eng. Sci.* **2016**, *141*, 28.
(58) Aparicio, L. M. Transient Isotopic Studies and Microkinetic Modeling of Methane Reforming over Nickel Catalysts. *J. Catal.* **1997**, *165*, 262.
(59) Falbo, L.; Martinelli, M.; Visconti, C. G.; Lietti, L.; Bassano, C.; Deiana, P. Kinetics of CO_2 methanation on a Ru-based catalyst at process conditions relevant for power-to-gas applications. *Appl. Catal., B* **2018**, *225*, 354.
(60) Xu, L.; Lian, X.; Chen, M.; Cui, Y.; Wang, F.; Li, W.; Huang, B. CO_2 methanation over CoNi bimetal-doped ordered mesoporous Al_2O_3 catalysts with enhanced low-temperature activities. *Int. J. Hydrogen Energy* **2018**, *43* (36), 17172.
(61) Garbarino, G.; Wang, C.; Cavattoni, T.; Finocchio, E.; Riani, P.; Flytzani-Stephanopoulos, M.; Busca, G. A study of $Ni/La\text{-}Al_2O_3$ catalysts: A competitive system for CO_2 methanation. *Appl. Catal., B* **2019**, *248*, 286.
(62) Hao, Z.; Shen, J.; Lin, S.; Han, X.; Chang, X.; Liu, J.; Li, M.; Ma, X. Decoupling the effect of ni particle size and surface oxygen deficiencies in CO_2 methanation over ceria supported Ni. *Appl. Catal., B* **2021**, *286*, 119922.
(63) Lin, S.; Hao, Z.; Shen, J.; Chang, X.; Huang, S.; Li, M.; Ma, X. Enhancing the CO_2 methanation activity of Ni/CeO_2 via activation treatment-determined metal-support interaction. *J. Energy Chem.* **2021**, *59*, 334.
(64) Siakavelas, G. I.; Charisiou, N. D.; AlKhoori, A.; AlKhoori, S.; Sebastian, V.; Hinder, S. J.; Baker, M. A.; Yentekakis, I. V.; Polychronopoulou, K.; Goula, M. A. Highly selective and stable Ni/La-M (M = Sm, Pr, and Mg)-CeO_2 catalysts for CO_2 methanation. *J. CO_2 Util.* **2021**, *51*, 101618.
(65) Iglesias, I.; Quindimil, A.; Mariño, F.; De-La-Torre, U.; González-Velasco, J. R. Zr promotion effect in CO_2 methanation over ceria supported nickel catalysts. *Inter. J. Hydrog. Energy* **2019**, *44* (3), 1710.
(66) Mears, D. E. Tests for transport limitations in experimental catalytic reactors. *Ind. Eng. Chem. Prod. Des. Dev.* **1971**, *10* (4), 541.
(67) Anderson, J. A criterion for isothermal behaviour of a catalyst pellet. *Chem. Eng. Sci.* **1963**, *18* (2), 147.
(68) Jangam, A.; Das, S.; Dewangan, N.; Hongmanorom, P.; Hui, W. M.; Kawi, S. Conversion of CO_2 to C1 chemicals: Catalyst design, kinetics and mechanism aspects of the reactions. *Catal. Today* **2020**, *358*, 3.
(69) Quindimil, A.; Onrubia-Calvo, J. A.; Davó-Quiñonero, A.; Bermejo-López, A.; Bailón-García, E.; Pereda-Ayo, B.; Lozano-Castelló, D.; González-Marcos, J. A.; Bueno-López, A.; González-Velasco, J. R. Intrinsic kinetics of CO_2 methanation on low-loaded Ni/Al_2O_3 catalyst: Mechanism, model discrimination and parameter estimation. *J. CO_2 Util.* **2022**, *57* (2022), 101888.
(70) Falconer, J. L.; Zağli, A. E. Adsorption and methanation of carbon dioxide on a nickel/silica catalyst. *J. Catal.* **1980**, *62* (2), 280.
(71) Dalmon, J.; Martin, G. A. Intermediates in CO and CO_2 hydrogenation over Ni catalysts. *J. Chem. Soc., Faraday Trans. 1: Phys. Chem. Condens. Phases* **1979**, *75*, 1011.

https://doi.org/10.1021/acs.iecr.2c00164
Ind. Eng. Chem. Res. 2022, 61, 10419−10435

(72) Ibraeva, Z. A.; Nekrasov, N. V.; Gudkov, B. S.; Yakerson, V. I.; Beisembaeva, Z. T.; Golosman, E. Z.; Kiperman, S. L. Kinetics of methanation of carbon dioxide on a nickel catalyst. *Theor. Exp. Chem.* **1991**, *26* (5), 584.
(73) Förtsch, D. On the basic effects on the gas composition governed by the water-gas shift equilibrium. *Energy* **2020**, *205*, 117883.
(74) Konishcheva, M. V.; Potemkin, D. I.; Badmaev, S. D.; Snytnikov, P. V.; Paukshtis, E. A.; Sobyanin, V. A.; Parmon, V. N. On the mechanism of CO and CO_2 methanation over Ni/CeO_2 catalysts. *Top. Catal.* **2016**, *59* (15), 1424.
(75) Aldana, P. A. U.; Ocampo, F.; Kobl, K.; Louis, B.; Thibault-Starzyk, F.; Daturi, M.; Bazin, P.; Thomas, S.; Roger, A. C. Catalytic CO_2 valorization into CH_4 on Ni-based ceria-zirconia. Reaction mechanism by operando IR spectroscopy. *Catal. Today* **2013**, *215*, 201.
(76) Solis-Garcia, A.; Louvier-Hernandez, J. F.; Almendarez-Camarillo, A.; Fierro-Gonzalez, J. C. Participation of surface bicarbonate, formate and methoxy species in the carbon dioxide methanation catalyzed by ZrO_2-supported Ni. *Appl. Catal., B* **2017**, *218*, 611.
(77) Yu, Y.; Bian, Z.; Wang, Z.; Wang, J.; Tan, W.; Zhong, Q.; Kawi, S. CO_2 methanation on $Ni\text{-}Ce_{0.8}M_{0.2}O_2$ (M = Zr, Sn or Ti) catalyst: Suppression of CO via formation of bridging carbonyls on nickel. *Catal. Today* **2020**, DOI: 10.1016/j.cattod.2020.07.049.
(78) Wang, F.; He, S.; Chen, H.; Wang, B.; Zheng, L.; Wei, M.; Evans, D. G.; Duan, X. Active site dependent reaction mechanism over Ru/CeO_2 catalyst toward CO_2 methanation. *J. Am. Chem. Soc.* **2016**, *138* (19), 6298.
(79) Jia, X.; Zhang, X.; Rui, N.; Hu, X.; Liu, C. Structural effect of Ni/ZrO_2 catalyst on CO_2 methanation with enhanced activity. *Appl. Catal., B* **2019**, *244*, 159.
(80) Boudart, M.; Mears, D.; Vannice, M. In congres international chimie industrielle. *Ind. Chim. Belge.* **1967**, *32*, 281.